2023-05-30

A Method of Reconstructing Historical Destructive Landslides Using Bayesian Inference

Raelynn Wonnacott
Brigham Young University

A Method of Reconstructing Historical Destructive Landslides Using Bayesian Inference

Raelynn Wonnacott

A thesis submitted to the faculty of
Brigham Young University
in partial fulfillment of the requirements for the degree of

Master of Science

Jared P. Whitehead, Chair
Benjamin Webb
Blake Barker

Department of Mathematics

Brigham Young University

ABSTRACT

A Method of Reconstructing Historical Destructive Landslides Using Bayesian Inference

Raelynn Wonnacott
Department of Mathematics, BYU
Master of Science

Along with being one of the most populated regions of the world, Indonesia has one of the highest natural disaster rates worldwide. One such natural disaster that Indonesia is particularly prone to are tsunamis. Tsunamis are primarily caused by earthquakes, volcanoes, landslides and debris flows. To effectively allocate resources and create emergency plans we need an understanding of the risk factors of the region. Understanding the source events of destructive tsunamis of the past are critical to understanding the these risk factors.

We expand upon previous work focusing on earthquake-generated tsunamis to consider landslide-generated tsunamis. Using Bayesian inference and modern scientific computing we construct a posterior distribution of potential landslide sources based on anecdotal data of historically observed tsunamis. After collecting 30,000 samples we find a landslide source event provides a reasonable match to our anecdotal accounts. However, viable landslides may be on the edge of what is physically possible. Future work creating a coupled landslide-earthquake model may account for the weaknesses with having a solely landslide or earthquake source event.

Keywords: Bayesian statistics, Markov chain Monte Carlo, inverse problems, earthquakes, tsunamis, seismic hazard analysis, submarine landslides

Acknowledgements

First, I would like to thank my parents, Courtney and Michael Wonnacott, for believing in me and pushing me forward since I was a child. I owe them more than I can express.

I would also like to thank my advisor, Jared Whitehead, who has both helped me to believe in my capability to achieve and has taken every opportunity to help me meet my goals. This support along with that of many others, including that of my committee members Benjamin Webb and Blake Barker, has been invaluable.

Next, I thank Taylor Paskett, Jake Callahan and Chelsey Noorda for their help on this project from debugging code to discussing ideas, with a special thanks to Dallin Stewart for collecting data and constructing prior distributions for this event. Additionally, my classmates and friends Matthew Steffen, Kolton Baldwin and Abigail Jenkins cannot go unnoted as they have provided unmatched friendship and support throughout the duration of both my undergraduate and graduate education.

Contents

List of Tables

List of Figures

Chapter 1. Introduction

On Friday, Sept. 28, 2018 a 7.5 magnitude earthquake was recorded in Central Sulawesi resulting in a tsunami. The tsunami was expected to be around 9.8 ft, 3 meters, high upon reaching Palu, the capital of Central Sulawesi. However, the narrow geography of the bay caused a nearly 20 ft, 6 meter, wave to hit the city of Palu. Local warnings were not issued and many were still on the beach as the tsunami struck. This tsunami ended up killing 1.5 million people. Indonesia is particularly prone to tsunamis and there is a strong need to understand the potential natural hazards of the region so that tsunami wave heights can be estimated and the proper warning systems put in place.

The majority of tsunamis in Indonesia are believed to be caused by earthquakes. One of the world's largest subduction zones is located along the Band Arc region of Indonesia. Subduction zones generate the world's largest earthquakes and the majority of large, destructive tsunamis [1, 2]. Despite the prominence of earthquake-generated tsunamis worldwide, accurate data for the years before the advent of the Cold War is not available due to a lack of instrumentation. Hence, the causes of some of the largest historical tsunamis are largely unknown, although they are most frequently hypothesized to stem from uplift from a significant earthquake. We focus on submarine landslides which are the second leading cause for tsunamis [3]. An analysis of landslide generated historical tsunamis is especially relevant as submarine landslides were not fully recognized as a means of tsunami generation prior to 1998. The 1998 Papua New Guinea event provided clear evidence of a landslide generated tsunami [4]. After the acceptance of submarine landslide tsunami generation, many tsunamis were reclassified as landslide generated. Among these were the 1929 Grand Banks tsunami [5], the 1979 Nice tsunami [6], and the 8150 BP Storegga landslide tsunami [7]. However, older historical records were written at a time when submarine landslides were not recognized as possible triggers and are potentially biased [8, 9].

Submarine landslides come in many shapes and forms. Slides can start on steep slopes

down to slopes of 1 degree. Average slide velocities range from 10 to 150 m/s (36 to 540km/hr) [10]. These slides can move large volumes of mass hundreds of kilometers. An extreme landslide event, the Storegga landslide, off the coast of Norway had a size of 5,600 km^3. This generated a tsunami in the North Atlantic Ocean with waves reacing 29km inland on several islands [7].

Additionally, an analysis of submarine landslide generated tsunamis in Eastern Indonesia is necessary as the Banda Arc region is home to the Weber Deep. Excluding trenches, this is the deepest point of the ocean in the world with a maximum depth near 7.2 km. This is thought to be created by a detachment fault. This fault created a gap of over over 60,000 sq km in the ocean floor [11]. This fault is called the Banda Detachment and is located between the volcanic and seismically active arcs. Slump scars have been measured along the Banda Detachment leading into the Weber Deep suggesting a frequent occurrence of landslides [11].

We focus on a tsunami occurring in 1852 along the Banda arc in Indonesia. This tsunami occurred before modern instrumental records so there is no seismometer reading to verify the magnitude and location of the potentially causal earthquake. However, an understanding of historical events, such as this one, is crucial to natural hazard assessment where the relevant temporal scales are hundreds to thousands of years [12]. We follow a novel approach presented by Ringer, et al.'s [12] group. This applied Bayesian inference to reconstruct the source earthquake parameters based on anecdotal accounts for this tsunami. We expand upon this approach to examine the hypothesis of a landslide generated tsunami for the same event.

Chapter 2. Background

2.1 Inverse Problems

The reconstruction of historical tsunamis is an inverse problem. Inverse problems arise in a large number of areas including medical imaging, remote sensing, signal processing, and

geosciences. In general, an inverse problem is any problem which seeks to determine parameters or initial conditions of a system based on observed measurements and the effect those observed values have on the system. These measurements most often are influenced by noise that can dilute the signal and/or provide extraneous information that is inconsistent. 'Solving' an inverse problem requires carefully inverting the parameter to signal map which is most frequently not a straightforward process. On the other hand, the forward problem will take a known set of parameters and initial conditions and evolve them forward to obtain observable outputs. While certainly not trivial, forward problems are typically much more approachable than inverse problems. In particular most models can have several combinations of parameters and initial conditions that can generate an identical set of observational outputs, implying that the inverse problem is ill-posed, i.e. one set of observations can be produced by multiple different sets of input parameters so that solutions of the inverse problem are rarely unique.

Regularization techniques provide one way to deal with the ill posedness of inverse problems. To introduce this we examine the equation

$$Ax \approx y \tag{2.1}$$

where H_1 and H_2 are seperable Hilbert spaces and $A : H_1 \to H_2$ is a compact operator. We know,

1) If a solution exists, it is unique if and only if $y \in R(A)$

2) The solution is unique if and only if $Ker(A) = 0$

Also, small errors (stochastic noise) in y may cause large errors in x. If either of these conditions, 1 or 2, is not met then the inverse problem (finding x from observing y) is ill-posed, whereas the forward problem (computing Ax for any given x) is always well defined.

We look at one regularization technique, Tikhonov regularization, which provides a solution to alleviate the two potential issues (existence and uniqueness of x given a specific y). As defined in [13]:

Definition 2.1. Let $\delta > 0$ be a given constant (typically small). The Tikhonov regularized

solution $x_\delta \in H_1$ is the minimizer of the functional

$$F_\delta(x) = ||Ax - y||^2 + \delta||x||^2,$$

provided that a minimizer exists. The parameter $\delta > 0$ is called the regularization parameter.

A common example of Tikhonov regularization is regularized least squares. Let A be an $m \times n$ matrix and let b be a vector in $\mathbb{R}^n$. The least squares problem can be described as $\text{argmin}_x ||Ax - b||^2$. When this system is underdetermined the least squares problem has infinitely many solutions and is ill posed. Adding a regularization term gives the problem $\text{argmin}_x ||Ax - b||^2 + \delta||x||^2$ which does have a unique solution and approaches the original problem as $\delta \to 0$.

Classical regularization techniques such as Tikhonov regularization provide a solution in the form of a single estimate. A further description of regularization techniques can be found in [13].

2.2 Stochastic or Bayesian Methods

In an attempt to consider the uncertainty involved in inverse problems, stochastic or Bayesian methods attempt to represent uncertainties using random variables. Bayes' rule is at the heart of most of these methods

$$p(\theta|d) = \frac{p(d|\theta)p(\theta)}{p(d)}. \tag{2.2}$$

We seek a posterior distribution, $p(\theta|d)$, which in our case summarizes what we know about the parameters θ of a source event given observational data, d (in our specific application these observations are the wave heights of a historical tsunami at various locations). We are unable to compute $p(d) = \int p(d|\hat{\theta})p(\hat{\theta})d\hat{\theta}$ as we cannot evaluate the probability of the observed tsunami across all potential source events. Instead we seek to find $p(\theta|d) \propto p(d|\theta)p(\theta)$. To evaluate our likelihood, $p(d|\theta)$, we create a forward model which takes our source event parameters (a model of the submarine landslide) and simulates a resultant tsunami. We then look at how closely our simulated tsunami matches the data from the historical ac-

count, assigning a likelihood probability to each such simulation. The prior distribution $p(\theta)$ incorporates expert knowledge about the source event (set of parameters that describe the submarine landslide). This primarily incorporates information about what is geographically feasible. In Section 5 and 6 we go over the likelihood and prior in more depth for landslide generated tsunamis. For a further discussion of the prior and likelihood for earthquake generated tsunamis see [12].

2.2.1 Variational Inference. Variational Bayesian methods provide a stochastic approach and are often used on otherwise intractable posterior distributions. These methods assume the posterior distribution comes from a specific family of distributions (typically parameterized by some finite set of parameters). This assumption allows the inference problem to be re-cast as an optimization problem where the optimal parameters are sought which allow the posterior to most closely approximate the observed data. Variational inference methods most commonly use Kullback-Leibler divergence to measure the difference between distributions. We call a realization of the family of distributions $q_\phi(\theta)$. In general the goal is to choose a variational family that is simple enough for efficient optimization but can capture a density close to the true posterior $p(d|\theta)$. Minimizing the KL divergence between the variational family and the posterior is equivalent to maximizing the Evidence Lower Bound (ELBO) with respect to $q_\phi(\theta)$

$$ELBO = \mathbb{E}_{q_\phi(\theta)}[\log p(d|\theta) - \log q_\phi(\theta)]. \tag{2.3}$$

Details on the derivation of the Evidence Lower Bound can be found in [14].

2.2.2 Sampling Methods. We choose to compute the posterior distribution using sampling methods to avoid the bias that can be introduced by hypothesizing a certain family of distributions will model the desired posterior. Markov chain Monte Carlo (MCMC) methods provide a way to sample from the posterior distribution, $p(\theta|d)$. Using this method we construct a Markov chain whose stationary distribution will converge to $p(\theta|d)$ in the limit

of large samples. Large but finite sampling from the Markov chain will yield a reasonable approximation of $p(\theta|d)$.

We construct the Markov chain using the Metropolis-Hastings algorithm [15, 16]. This is an iterative algorithm. It creates a Markov chain with transition probability, outlined in steps ii and iii below, which ensures $p(\theta|d)$ satisfies the detailed balance equations and is the stationary distribution of the chain. Conveniently, this method only requires the evaluation of the probability density function up to a constant of proportionality (no need to compute the denominator in Bayes' Theorem). This is necessary in our case as we are unable to compute the normalization constant $p(d)$.

A brief overview of the Metropolis-Hasting algorithm is provided here:

(i) To begin, we choose an initial sample, θ_0.

(ii) Using a proposal distribution, $q(\cdot|\theta_t)$, we propose a potential sample θ_{t+1}, given our current sample θ_t.

(iii) New samples are accepted or rejected according to the acceptance probability α, defined in Algorithm 1, which ensures we achieve the desired stationary distribution [13].

(iv) Steps (ii) and (iii) are repeated until the desired number of samples is drawn from the distribution.

Algorithm 1 Metropolis-Hastings

for t in 1, 2, ... **do**
  Draw $x \sim q(.|\theta_t)$
  Set $\alpha = \min(1, \frac{p(x|d)p(x)}{p(\theta_t|d)p(\theta_t)} * \frac{q(\theta_t|x)}{q(x|\theta_t)})$
  Draw $u \sim \text{unif}(0, 1)$
  if $u \leq \alpha$ **then**
    $\theta_{t+1} = x$
  else
    $\theta_{t+1} = \theta_t$
  end if
end for

In our case, we choose $q(\cdot|\theta_t)$ to be Gaussian. This is a form of random walk MCMC as our proposal distribution is symmetric. Since $q(\theta_t|x) = q(x|\theta_t)$ we have $\alpha = \min(1, \frac{p(x|d)p(x)}{p(\theta_t|dp(\theta_t)})$.

2.3 Mixture Models

Mixture models are probabilistic models that consist of a combination of distributions. Mixture models are examples of latent variable models. A latent variable model occurs when P(Z), for a random variable Z, is really a marginal distribution, P(Z,X), where X is a latent or unobserved random variable. Here, $X \sim \text{Cat}(\pi)$ where $\pi = (\pi_1...\pi_j)$, $\sum_{j=1}^{J} \pi_j = 1$ and $\text{Cat}(\pi)$ represents a categorical distribution, where each category is associated with probability π_i. Each category corresponds to a distribution in the mixture model. In order to sample from a mixture model one first draws a sample from $\text{Cat}(\pi)$ and then samples from the corresponding distribution X.

$$P(X = x) = \sum_{j=1}^{J} P(X = x|Z = j)P(Z = j) = \sum_{j=1}^{J} p_j(X = x)\pi_j. \tag{2.4}$$

These p_j can be any probability density function. A further reference on latent variable/mixture models can be found in [17].

We refer back to this in the construction of the prior. For the construction of the prior each 'category' corresponds to a previously recorded landslide event. We use a Gaussian mixture model to place higher probability on samples that are close to landslide events that have been previously recorded. Details can be found in Chapter 6.

Chapter 3. Dual Hypotheses Bayesian Inversion

One of the shortcomings of deriving the posterior according to (2.2) is that we obtain relative probabilities, i.e. we do not actually compute the denominator present in Bayes' Theorem. However, we still desire a quantifiable way to compare two or more hypotheses with separate

posterior distributions. For example, we eventually want to compare the relative probability of a historically observed tsunami being sourced directly from an earthquake relative to a submarine landslide (or perhaps even a combination of these two potential sources). To accomplish this we use an approach based on binary classification. To demonstrate this method, as well as motivate work on landslide generated tsunamis, we return to previous results for earthquake generated tsunamis. This discussion relies on the work of Paskett et al. [18].

3.1 1820 South Sulawesi event

In 1820 there was an earthquake near southwest Sulawesi in central Indonesia which lead to a destructive tsunami that spread from Bulukumba on South Sulawesi Island to Sumenep on East Java, a distance of over 700 km. This event is unique as there were two potential sources for the tsunami, the Flores back-arc thrust and the Walanae Fault (parallel to Selayar Island) shown in Figure 3.1. Each of these faults represent a very distinct hypothesis and produce two posterior distributions defined on different parameters so that a direct comparison between the two is impossible, see [18] for details. We summarize the method and results found in [18] with the dual posterior distributions as seen in Figure 3.2.

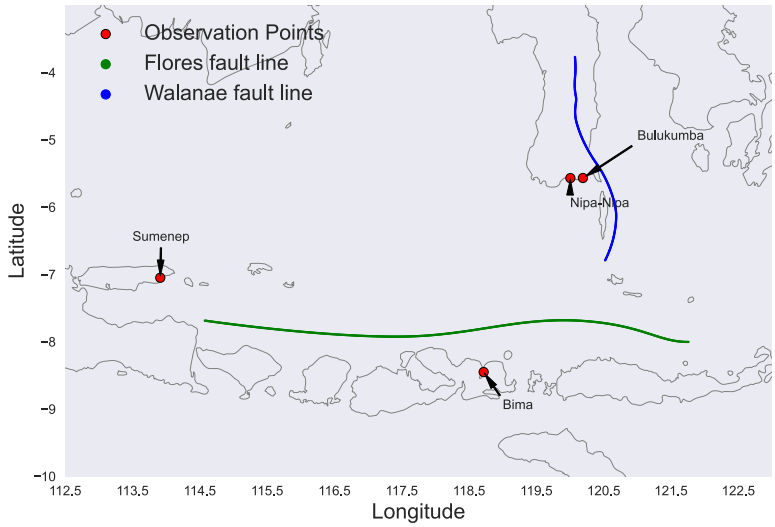

Figure 3.1: A depiction of the latitude longitude placement of the Walanae/Selayar Fault (blue) and Flores Thrust (red). The tsunami observations are shown in red. of the Flores thrust).

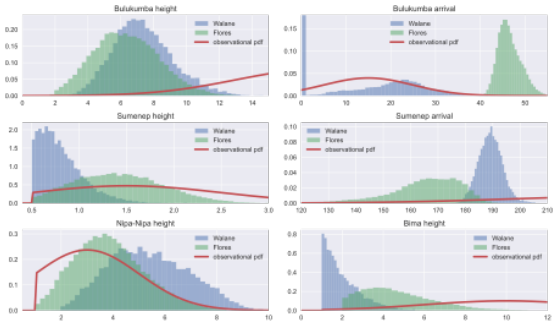

(a) Wave Height/Arrival Time Posterior

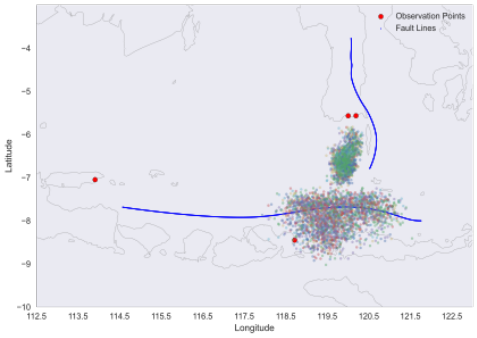

(b) Longitude Latitude Posterior

Figure 3.2: (a): Posterior for wave heights and arrival times corresponding to the Walanae (blue) and Flores (green) faults. The selected observational probabilities that were determined to best match the historical account are shown in red. (b): Locational posterior for both the Flores (primarily East/West) and Walanae (primarily North/South) faults.

Looking at the posterior distributions we see that seismically speaking Walanae is a better fit. Earthquakes along the Flores fault matching the data require a magnitude of about 8.8 Mw which is on the upper limit of what the fault is able to support. The posterior for Walanae, while still leaning toward a higher magnitude, is more physically feasible. Samples

from the Walanae fault also more closely match Bulukumba arrival times and are closer to the arrival time at Sumenep (although neither fault seems to match this perfectly).

3.2 Classifier

In order to make a quantifiable (as opposed to the heuristic description provided above) comparison between the two faults we use a binary classifier. Input to the classifier consists of the 6 observational quantities depicted in 3.2 (a): 4 wave heights and 2 arrival times. This input data is divided into two classes defined by the originating fault (Walanae or Flores). Specifically we use data from the 104,970 tsunami simulations originating from the Walanae fault and the 127,690 simulations originating from the Flores thrust, i.e. the observed values are the data and the originating fault is the label for the classifier.

Before training the classifier, we remove samples that do not have a finite log posterior and use a 30-70 test train split. This leaves us with a training set consisting of 89,554 Flores samples and 73,308 Walanae samples. Our test set contains 38,136 Flores samples and 31,662 Walanae samples.

We trained a binary logistic XGBoost and random forest classifier. With default settings the classifiers obtained accuracies of 99.993% and 99.996% respectively on the test set. Next, we use these classifiers on samples drawn independently from our observational probabilities (the red curves depicted in Figure 3.2 (a)). Out of 1 million samples the random forest classifier selected Walanae as the source 94.4% of the time and the logistic regression classifier selected Walanae 98.4% of the time.

Interpreting this result, we would claim that under the hypothesis that the 1820 tsunami was caused by either an earthquake along Flores or Walanae faults, we would be 94.4% to 98.4% confident that the source was the Walanae fault. We emphasize at this point that the binary classification approach taken here to distinguish between two different hypothesized sources is a unique contribution to inverse problems and the Bayesian approach in general.

Although we believe the Walanae fault to be more likely than the Flores thrust as the

source, it does not fit as well as expected with our observations. In particular the observed wave heights at Bulukumba are significantly larger than any of the simulations we performed for either type of earthquake source. A local landslide near Bulukumba in addition to the earthquake may account for the discrepancy between our simulated wave heights and observations as landslide generated tsunamis are typically more localized (explaining the disparity between the wave heights at Bulukumba and all other locations). In order to simulate an event like this we must first create a method similar to that employed in [12] that is capable of examining submarine landslides as opposed (or in addition) to earthquakes. The first step in this process is to create a forward model which simulates a tsunami from landslide parameters.

Chapter 4. Forward Model

For the forward model we use a very simplified landslide model. Although more robust models exist we cannot justify inferring the parameters of a complicated system/model with anecdotal data. Here we seek to balance simplicity with a reasonable degree of physical principles. We choose a model with the parameters listed in Table 4.1. This means the height of the tsunami wave depends only on the dimensions of the landslide body, the bathymetry, and the initial velocity.

Trainable Parameters	**Description**
d	Thickness
V	Volume
v_0	Initial Velocity
ar	Aspect Ratio
Fixed/Bathymetry Based Values	**Description**
p_s	density of dirt
p_w	density of water
g	gravity
θ	angle of slope
C_F	surface skin friction
f	Coulomb friction

Table 4.1: Model Parameters

We discuss the forward model in two parts: First, we model the sea floor deformation resulting from the slide. This is then passed to the a software package, GeoClaw, [19, 20, 21, 22] which propagates tsunami waves via solving the fully nonlinear two-dimensional shallow water equations via a Finite Volume discretization with an adaptive temporal and spatial grid.

4.1 Sea Floor Deformation

As illustrated in Figure 4.1 we model the seafloor deformation by modeling the landslide as a solitary block of material. The motion of this block is derived in terms of its center of mass and then the block is moved in accord with the movement of the center of mass.

4.1.1 2d-Model. Motion of the center of mass is based on the following governing equation of landslide motion [23, 9].

$$p_s V \frac{\partial u}{\partial t} = (p_s - p_w) g V [\sin(\theta) - f \cos(\theta)] - p_w \frac{C_F l d}{2} u^2. \tag{4.1}$$

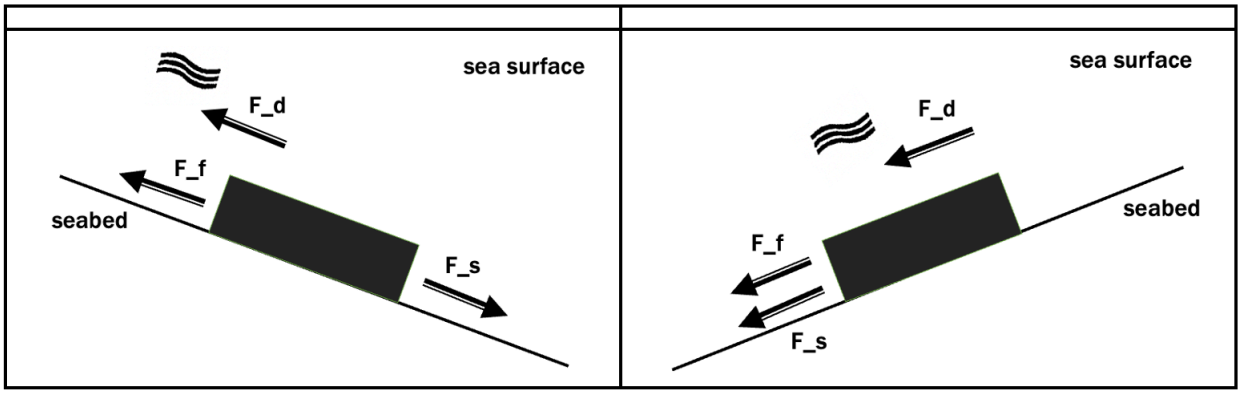

(a) Forces Upslope (b) Forces Downslope

Figure 4.1: (a): Depiction of the forces on a block landslide moving upslope. (b): Depiction of the forces on a block landslide moving downslope.

This equation models landslide motion down slope on an inclined plane. Equation 4.1 is of the form $F = ma$ following Newton's 2nd Law. Here the forces involved are the rolling down force $F_s = (p_s - p_w) g V \sin(\theta)$, the sliding friction force (the resistance to motion of the seafloor against the landslide block) $F_f = (p_s - p_w) g V f \cos(\theta)$, and the drag coefficient $F_d = p_w \frac{C_F l d}{2} u^2$ (the drag of the water being pushed by the landslide block). We have mass $p_s V$ and acceleration $\frac{\partial u}{\partial t}$. For our model we also need to simulate how the mass of the landslide slows as it moves uphill. To do this we only need change the sign of our rolling down force as shown in Figure 4.1. Hence, equation (4.1) becomes

$$p_s V \frac{\partial u}{\partial t} = (p_s - p_w) g V [-\sin(\theta) - f \cos(\theta)] - p_w \frac{C_F l d}{2} u^2. \tag{4.2}$$

For simplicity we rewrite (4.1) as

$$a \frac{\partial u}{\partial t} = b - c u^2, \tag{4.3}$$

where

$$a = (p_s + p_w V_w), \quad b = (p_s - p_w) g V [\sin(\theta) - f \cos(\theta)], \quad c = p_w \frac{C_F l w}{2}.$$

Similarly, we write (4.2) as

$$a\frac{\partial u}{\partial t} = b - cu^2, \tag{4.4}$$

where this time

$$a = (p_s + p_w V_w), \quad b = (p_s - p_w)gV[-\sin(\theta) - f\cos(\theta)], \quad c = p_w \frac{C_F l w}{2}.$$

In order to use (4.1) and (4.2) to determine the motion of our landslide we must solve for the velocity and position of the landslide block. The solution to (4.3) and (4.4) breaks into the following cases.

$$u(t,\theta,v_0) = \left\{ \begin{array}{ll} \frac{-\sqrt{-b}\tan(\frac{\sqrt{-bc}t}{a} - \arctan(\frac{\sqrt{c}v_0}{\sqrt{-b}}))}{\sqrt{c}}, & b < 0 \\ \\ \frac{\sqrt{b}\tanh(\frac{\sqrt{bc}t}{a} + \operatorname{arctanh}(\frac{\sqrt{c}v_0}{\sqrt{b}}))}{\sqrt{c}}, & b \geq 0, v_0 < \sqrt{\frac{b}{c}} \\ \\ \frac{\sqrt{b}\coth(\frac{\sqrt{bc}t}{a} + \operatorname{arccoth}(\frac{\sqrt{c}v_0}{\sqrt{b}}))}{\sqrt{c}}, & b \geq 0, v_0 > \sqrt{\frac{b}{c}} \end{array} \right\},$$

where the solution $u(t,\theta,v_0)$ gives us the velocity moving down a slope with angle θ after t seconds. In order to get the distance moved over an interval of time we numerically integrate u using Simpson's rule [24].

4.1.2 3d-Model. Up to this point we have dealt with down/up slope movement in 2-d. We now expand this model to work in a 3-d setting by moving along lattitude and longitude lines, i.e. the horizontal motion has two dimensions. First we need an initial velocity in both directions. The initial velocity is split up between latitude and longitude based on the gradient of the slope in each respective direction. Initial velocity begins movement in the downhill direction and the lat/lon slope is calculated at the starting point. Then the distance moved after t seconds in each of the latitude and longitude directions is calculated based on our 2-d model. After t seconds the slope at the new position is calculated. Initial velocity in the lat/lon position is the respective ending velocity from the previous time step. This process is repeated iteratively either a preset finite number of times or after velocity

drops below a threshold (when the norm of the velocity vector drops below 10 m/s).

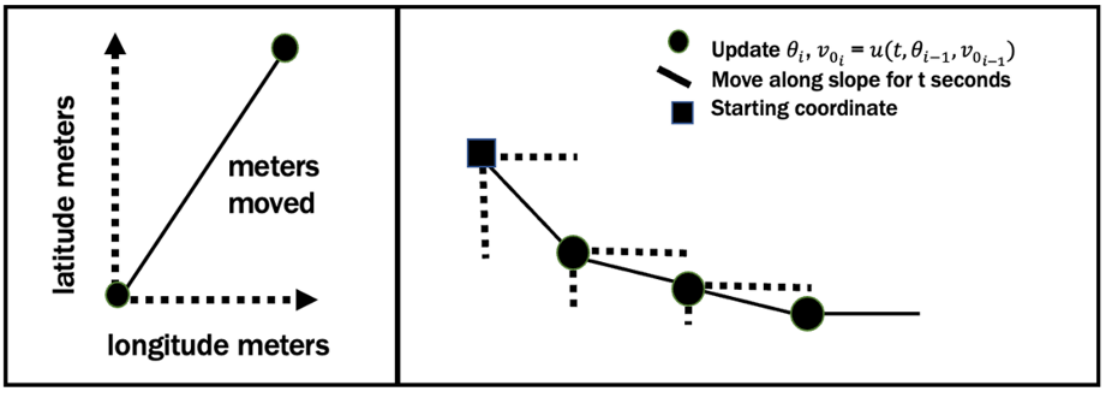

(a) Distance Moved in a Single Step (b) Distance Moved After Multiple Steps

Figure 4.2: (a): Depiction of the total meters moved in a single step. This is based off of the calculated meters moved in both longitude and lattitude directions. (b): Depiction of the meters moved after multiple steps. The initial latitude/longitude velocity for each step is based off of respective final latitude/longitude velocity of the previous step. Additionally, the angle of the slope in the latitude and longitude direction is calculated at each step.

The following pseudo-code provides a summary of the center of mass movement of the landslide in 3-d.

Algorithm 2 Center of Mass Movement Pseudocode

Define $\triangle$ based on grid spacing

Choose start coordinates

while velocity $<$ threshold **do**

 # get elevation at current coordinates

elev = bathymetry[coord[0],coord[1]]

#get lat/lon elevation offsets

elev1 = bathymetry(coord[0] + $\triangle$, coord[1])

elev2 = bathymetry(coord[0] - $\triangle$, coord[1])

elev3 = bathymetry(coord[0], coord[1] + $\triangle$)

elev4 = bathymetry(coord[0], coord[1] - $\triangle$)

 # find lat/lon angle of slope

theta_lon = $\arctan(|\text{elev1} - \text{elev2}|/(2\triangle))$

theta_lat = $\arctan(|\text{elev3} - \text{elev4}|/(2\triangle))$

 # determine if we are moving up or downslope (this determines

if u will be based on equation 4.1 or 4.2)

 # find distance moved in lon/lat direction using simpson's rule

dist_lon = simpson(u(t,theta_lon,v_0_lon))

dist_lat = simpson(u(t,theta_lat,v_0_lat))

 # update initial velocity

v_0_lon = $u(\text{seconds}, \text{theta\_lon}, v_0\text{\_lon})$

v_0_lat = $u(\text{seconds}, \text{theta\_lat}, v_0\text{\_lat})$

 # project distance on the slope to the grid and update coordinates

coord[0] = coord[0] + proj(dist_lon)

coord[1] = coord[1] + proj(dist_lat)

end while

There are two stopping criterion for this model:

(i) **When the velocity is under a threshold.** Note, when moving uphill at a slow velocity the mass of the landslide may begin to move backwards, in the opposite direction of our initial velocity. In this case we set our velocity to zero. This prevents mass from sloshing back and forth as the slide comes to a stop. This is reasonable as we are not considering changes to the block of mass as the landslide evolves, i.e. in reality the landslide would lose mass and form as it evolves.

(ii) **After 10 minutes.** This is mainly for computational reasons, but is justified as tsunami wave heights are primarily determined by the initial movements of the slide, i.e. the primary and dominant wave is created from the initial movement and later motion has a much less significant effect.

After we have determined the center of mass movement as outlined above, we take a discrete number of centers and place a 'box of mass' in the appropriate dimensions around that center of mass. The length of the box is perpendicular to the direction of motion, and the width is parallel to the motion.

Model output for a slide with length width and thickness set respectively to 40km, 15km, and 50m is shown in Figure 4.3. The slide depicted here has an initial velocity of 25 m/s and starts at longitude, latitude values of $(131.7, -5)$.

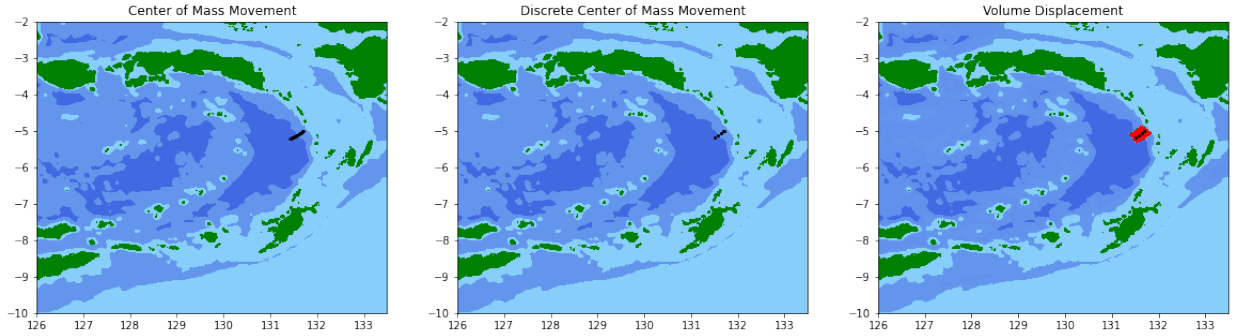

Figure 4.3: (Left): Depiction of the center of mass movement of the landslide during a ten minute period. (Center): Location of the slide every 120 seconds creating five discrete steps. (Right): Volume of the landslide added around the center of mass at 5 discrete steps.

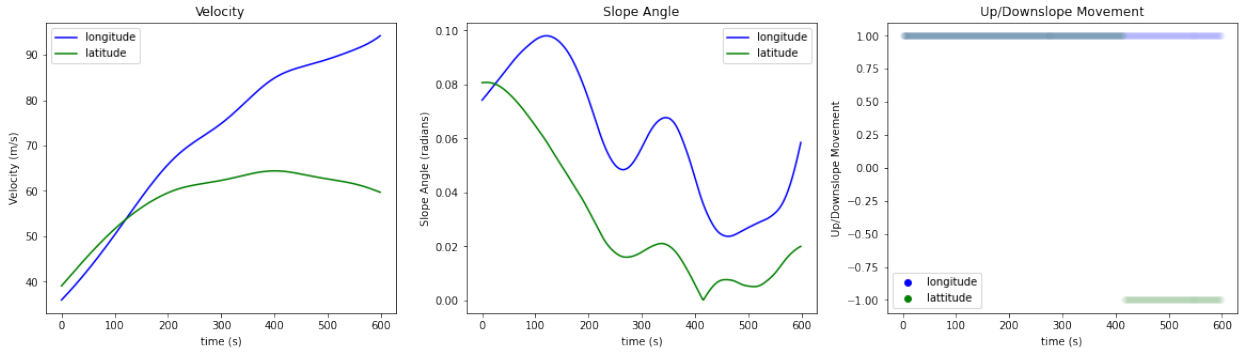

Figure 4.4: (Left): Velocity of the slide shown over the initial ten minute period. Longitude/Latitude velocity is shown in blue/green. (Center): Angle of descent over initial ten minute period of the slide. (Right): Depiction of whether the slide is moving up or down hill. Downhill movement occurs when value is one and uphill movement occurs when value is negative one. We see the latitude velocity begin to slow at four hundred seconds as the slide begins to move uphill.

4.2 Tsunami Propagation

The output of the model from the previous section is then fed into the Geoclaw software package which propagates tsunami waves. Waves corresponding to the landslide shown in Figure 4.3 are shown in Figure 4.5.

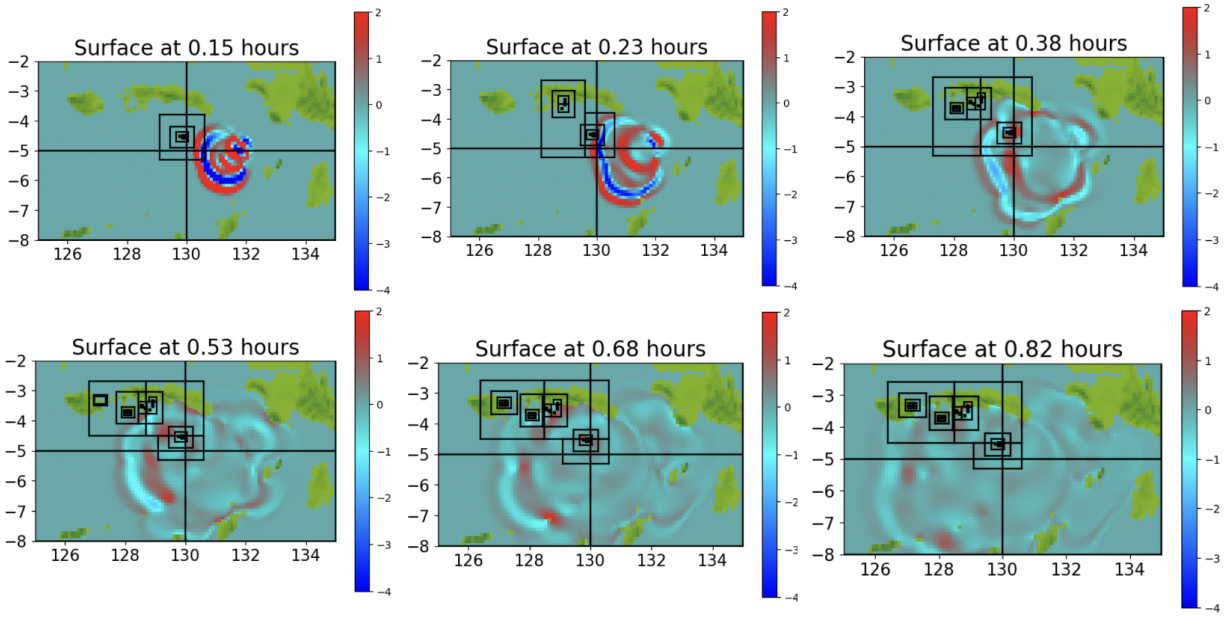

Figure 4.5: Tsunami wave propagation of the submarine landslide shown in Figure 4.3.

Chapter 5. Likelihood

5.1 Observations

Our likelihood is based on observations from the 1852 Banda Arc tsunami. Observations come from anecdotal accounts found in the Wichmann catalog [25, 26]. Thirteen observations are detailed enough to provide quantifiable information on our tsunami. These accounts span nine locations, shown in Figure 5.1.

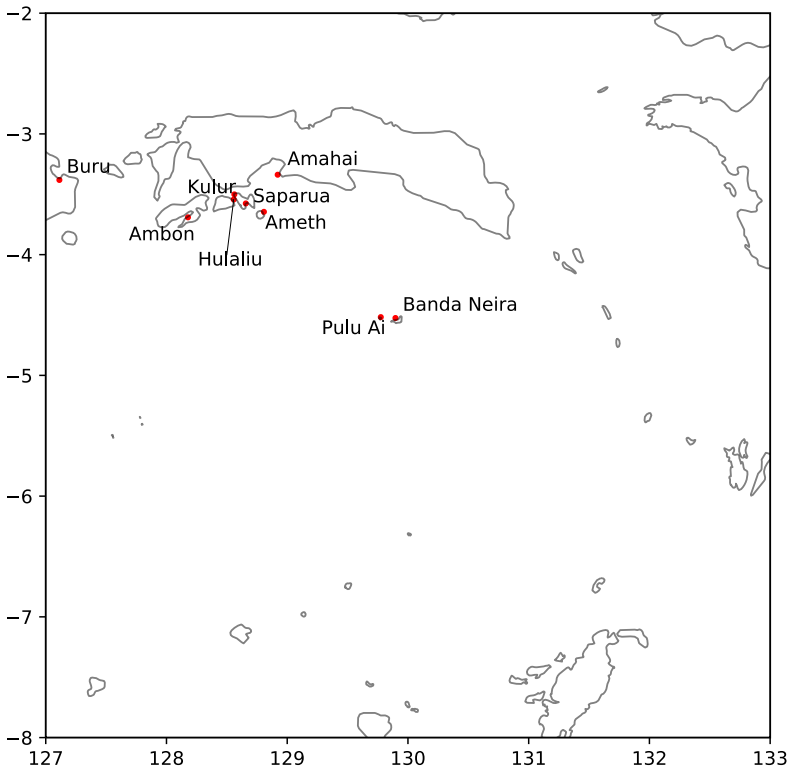

Figure 5.1: Observation locations for the Nine observation locations found in the Wichmann catalog.

Observations taken from the catalog provide information on:

- **Arrival time**. The arrival time of the first non trivial wave from the start of the landslide.
- **Wave height**. The maximum wave height. Wave heights were recorded at all nine locations.
- **Inundation length**. The distance inland that the wave traveled onshore.

We recognize that a lack of modern measurements adds additional uncertainty in our problem. We develop a distribution for each observation which gives the probability of an

observation corresponding to specific values. Distributions for each observation are shown in Figure 5.2. To illustrate the process for creating observational distributions, we present one example location in detail.

5.1.1 Sample Observational Account: Banda Neira. We do not go through observational accounts for each wave height but demonstrate the process for a single observation.

Page 242 in the Wichmann catalog provides an observation of the tsunami at Banda Neira: "Barely had the ground been calm for a quarter of an hour when the flood wave crashed in...The water rose to the roofs of the storehouses and homes...[the wave] reached the base of the hill on which Fort Belgica is built on Banda Neira". From this account we find:

- **An arrival time**. "A quarter of an hour". Based on observations from this and other locations we are assuming that the submarine landslide was caused by an earthquake (although not necessarily a subduction zone megathrust event as considered in [12]). Observations record arrival times after shaking subsides. The historical record indicates that the shaking lasted about 5 minutes and the landslide could have occurred at any point in this interval. We construct our likelihood with a skew toward longer arrival times with a mean of 15 minutes. Our final distribution is a skew-normal distribution with a mean of 15 minutes, standard deviation of 5 minutes, and skew parameter of 2.

- **A wave height**. "The roofs of the storehouses and homes". Based on the standard construction of the time, most buildings were on stilts with high vaulted roofs. In addition this observation occurred on a morning of exceptionally low tide. Hence we estimate a height of about 6.5 meters. For our likelihood we create a normal distribution with a mean of 6.5 meters with standard deviation of 1.5 meters. Thus waves from 3 to 9 meters have a reasonable probability.

- **An Inundation length**. "The water reached the base of the hill on which Fort Belgica is built". To quantify this account, 20 points along the beach were randomly selected

and the distance between each point and the base of the hill was calculated using ARCGIS. We choose our likelihood to be a normal distribution with a mean of 185 meters and a standard deviation of 65 meters corresponding to the mean and standard deviation of our measurements.

5.2 Observational Probabilities

In a similar manner we quantify accounts from the other 8 locations. The resultant distributions are treated independently as the actual dependence of each observation is unknown and indeed very difficult to ascertain. Hence, we compute the total likelihood as the product of each observable likelihood.

$$P(D|\theta) = \prod_{i=1}^{13} L_i(G(\theta)), \tag{5.1}$$

where $G(\theta)$ represents the output of our forward model for sample θ and L_i represents our ith observational distribution. For a further discussion of the likelihood see [12].

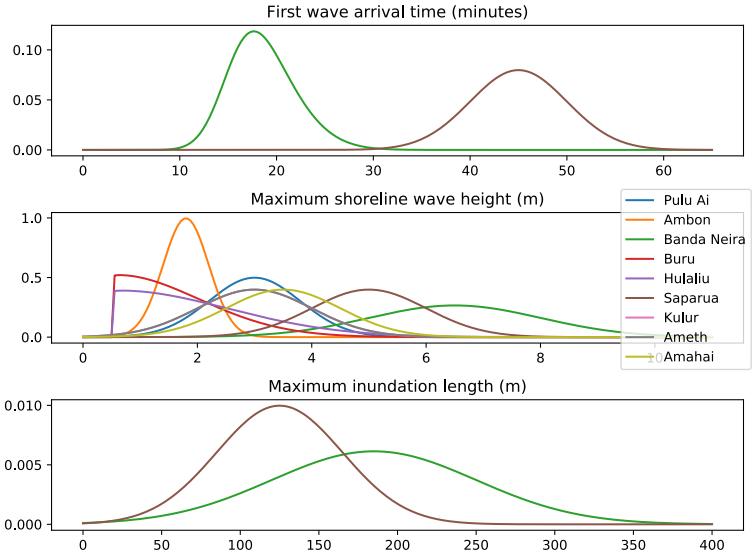

Figure 5.2: All 13 observational distributions.

Chapter 6. Prior Probabilities

We construct prior distributions based on data from past submarine landslides. As opposed to both earthquakes and arial (above sea) landslides, submarine landslides are not easily accessible (or often even noticeable) to modern measurement equipment. What we do know about submarine landslides often comes from costly oceanographic surveys [27]. As a result there exists surprisingly limited data on submarine landslides, particularly those capable of producing a tsunami of the magnitude in this investigation.

We rely on available literature and physical knowledge to construct the prior distributions. The prior distributions are built from 33 events from 14 sources [4, 8, 9, 28, 29, 30, 31, 32, 33, 34, 35, 36, 37, 38] which mainly supply information on landslide volume and thickness. Data includes landslide records from all over the world and is supplemented by sources from highly detailed numerical simulations. We construct the prior on volume and thickness using this data. Additionally, we create priors for initial velocity, and latitude/longitude. We need to convert volume as seen in the prior to width and length for the forward model and so create and search over a prior for aspect ratio as well. For priors that are not data based (initial velocity, latitude/longitude and aspect ratio) we rely on bounds discussed with geophysicist Steven N. Ward.

We treat the model parameters as if they are independent and so the prior distribution for a sample θ is defined to be the product of the prior probability for each parameter,

$$P(\theta) = \sum_{j=1}^{5} p_j(\theta_j). \tag{6.1}$$

6.0.1 Volume. The volume of the submarine landslide is correlated to the slope of the descent. We use data collected on the volume and slope of submarine landslides shown in Table 6.1 to construct the prior distribution on volume. The prior distribution for volume is a defined as a Gaussian mixture model

$$P(\theta_i) = \sum_{j=1}^{21} N(\theta_i, \mu = d_j, \sigma = 4)\pi_j. \tag{6.2}$$

Slope (°)	1.21	1.45	1.92	1.03	0.62	0.72	0.91
	0.75	1.08	0.72	2.03	1.33	0.28	0.28
	1.49	1.53	3.98	4.96	1.19	2.16	7.09
Volume (km^3)	1.5	1.5	0.216	1.261	7.064	4.26	34.386
	7.134	27.932	55.571	.037	.011	33.009	16.951
	4.400	.718	20.563	3.142	.005	20.000	.005

Table 6.1: Data for Volume Prior.

Here, π is chosen to place equal emphasis on each distribution and d_j represents the jth data point from the collected data in Table 6.1. Volumes that have been recorded, or are close to volumes of recorded events have greater prior probability.

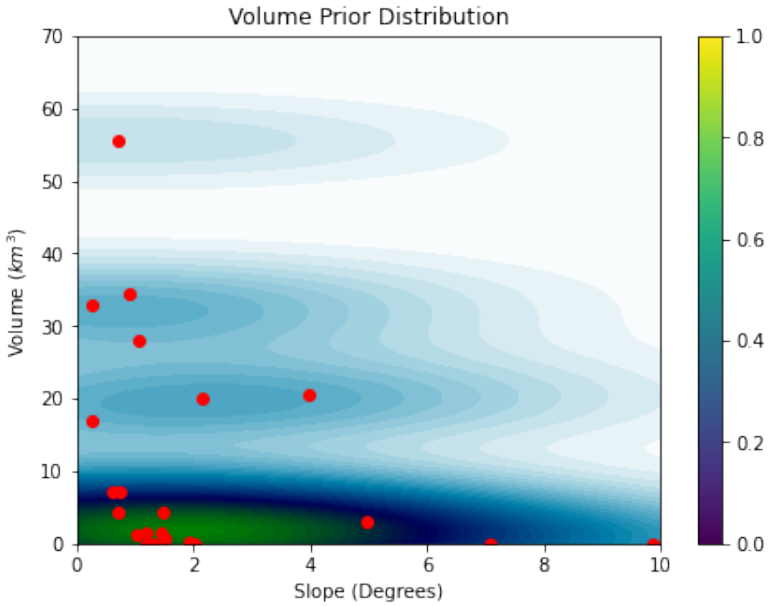

Figure 6.1: Prior for the volume of a submarine landslide. Red points represent previously recorded volumes for submarine landslide events. These points are found in Table 6.1. A Gaussian distribution is placed around each point in the construction of the prior.

6.0.2 Aspect Ratio. We determine length and width from volume and thickness using an aspect ratio parameter. The prior distribution for the aspect ratio is uniform from .3 to 1. This ensures the length of our slide is always perpendicular to the direction of movement and the width is not so small as to be unrealistic.

6.0.3 Thickness. We use the data in Table 6.2 to create a prior on the thickness of submarine landslides. This prior is constructed similarly to the prior on volume using a Gaussian mixture model

$$P(\theta_i) = \sum_{j=1}^{10} N(\theta_i, \mu = d_j, \sigma = 10)\pi_j. \tag{6.3}$$

Again, π is chosen to place equal emphasis on each distribution and d_j represents the jth data point from Table 6.2.

Thickness (m)	25	35	30	30	75	90	10	100	130	350

Table 6.2: Data for Thickness Prior.

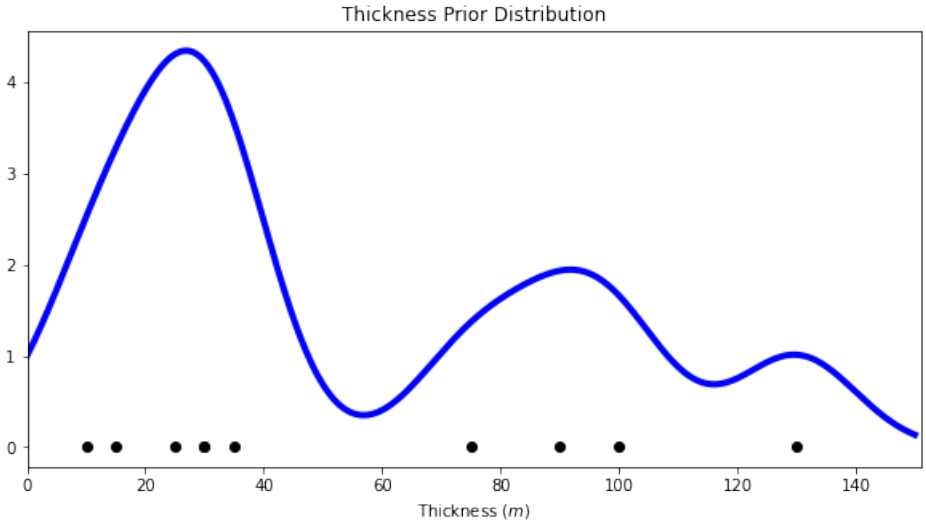

Figure 6.2: Prior distribution for the thickness of a submarine landslide. Black points represent values for recorded submarine landslide events. These points are found in Table 6.2. A Gaussian distribution is placed around each point in the construction of the prior.

6.0.4 Initial Velocity. Submarine landslides are most often triggered by earthquakes (which is the hypothesized source in this situation), however there are many forces that can cause unstable slopes to fail. We do not model events preceding a submarine landslide but instead incorporate this information into the slides initial velocity. An earthquake generated landslide may have a higher initial velocity than a slide caused by sediment which increasingly

becomes more unstable over time, or even a slide that occurs moments after an earthquake destabilizes the sediment. The prior distribution for initial velocity is uniformly distributed between 10 and 100 m/s or 36 to 360 km/hr.

6.0.5 Latitude/Longitude. Our prior distribution for Latitude and Longitude is based on depth. Landslides occuring at a shallower depth are more likely to cause a tsunami. Landslides that begin in the deep ocean may not create a disturbance at the waters surface, or the resultant disturbance will be so small that no noticeable wave will be produced. We generate the following prior distribution for depth which is in turn used as the prior distribution for latitude and longitude as the depth of the initial position of the slide depends on its geographic location.

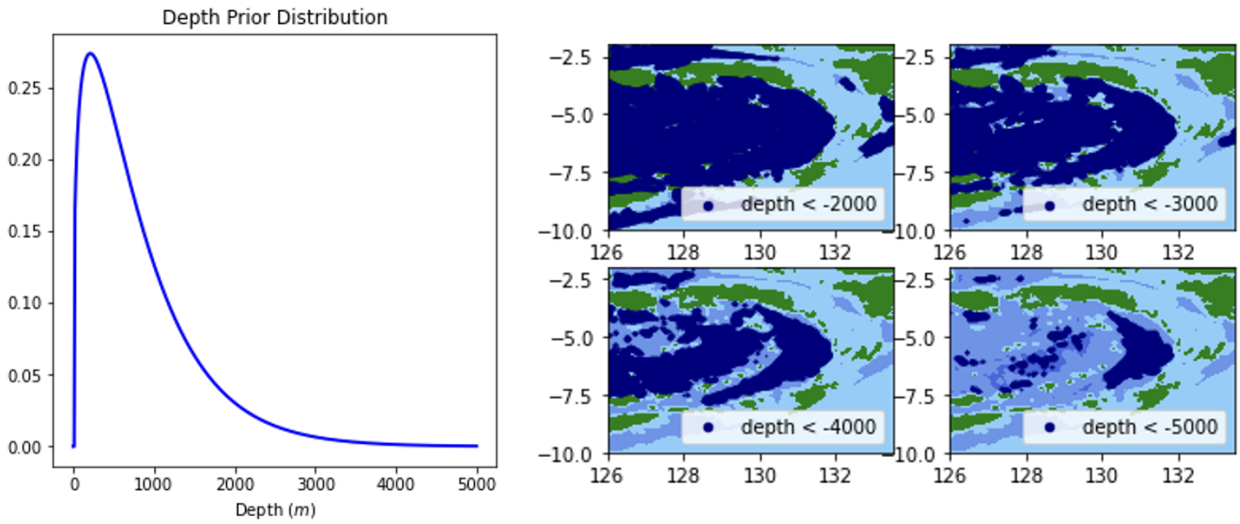

Figure 6.3: (Left): Prior distribution for the depth of a submarine landslide. Landslides starting at a shallow depth are more likely to disturb the water's surface and have a higher prior probability. (Right): Latitude/longitude points below a certain depth and hence prior probability are shown in navy.

Chapter 7. Results

In order to sample from the posterior distribution we initiated 10 different MCMC chains. These ran simultaneously on BYU's supercomputer in the Office of Research Computing. The majority of computational expense came from the propagation of the tsunami waves to the gauge locations. This was done by the software package GeoClaw. GeoClaw runs in parallel on 24 cores. In total, a single simulation using the forward model takes between 5.5 and 9 minutes. This is dependent on the cluster the job is assigned. Samples for the landslide model take longer than the earthquake model where a single sample took less than two minutes. The earthquake results in instantaneous deformation of the sea floor on one occasion. The landslide model updates the deformation of the sea floor on five occasions over a ten minute period. However, the landslide model is much faster than the earthquake model for the 1820 event, which had slower computational time arising from the difficulty of a dual fault rupture. For this event a single sample took approximately 12 minutes.

These chains were started at 6 different longitude-latitude locations as seen in Figure 7.1. All of the other initial parameter values for each chain can be found in Table 7.1. The majority of chains start with a volume of $30,000,000,000m^3$ ($30km^3$) and an aspect ratio of .375. This is because numerical simulations by [11] found the landslide that best matched observational data was 40 km long by 15 km wide with 50m thickness. Chains 9, and 10 have a reduced volume and initial velocity when compared with the other chains because these initial points had such a high proximity to Banda Neira. The original volume of 30 km^3 created a wave large enough, approximately 40 ft upon arrival at Banda Neira, to caused numerical instability, by violating CFL conditions, in the tsunami propagation model. To simulate these large waves we would need to significantly decrease our timestep increasing the computational cost. However, the waves that were large enough to cause instability are also too large to match the data so we can simply adjust the initial parameters accordingly.

	Lattitude	Longitude	Initial Velocity	Volume	Thickness	Aspect Ratio
Chain 1	-6.2	130	25	30000000000	50	.375
Chain 2	-6.2	130	75	30000000000	50	.375
Chain 3	.-5	131.7	25	30000000000	50	.375
Chain 4	.-5	131.7	75	30000000000	50	.375
Chain 5	.-6.3	131.7	25	30000000000	50	.375
Chain 6	.-6.3	131.7	75	30000000000	50	.375
Chain 7	-7.2	130.3	25	30000000000	50	.375
Chain 8	-7.2	130.3	75	30000000000	50	.375
Chain 9	-4	130.5	15	10000000000	50	.375
Chain 10	-5	130.4	15	15000000000	50	.375

Table 7.1: Starting parameters for all 10 chains.

Initial slides are shown in Figures 7.1, 7.2 and 7.3. The initial velocities of the initial landslides are dependent on the friction coefficients f, and C_D in the equation governing landslide motion.

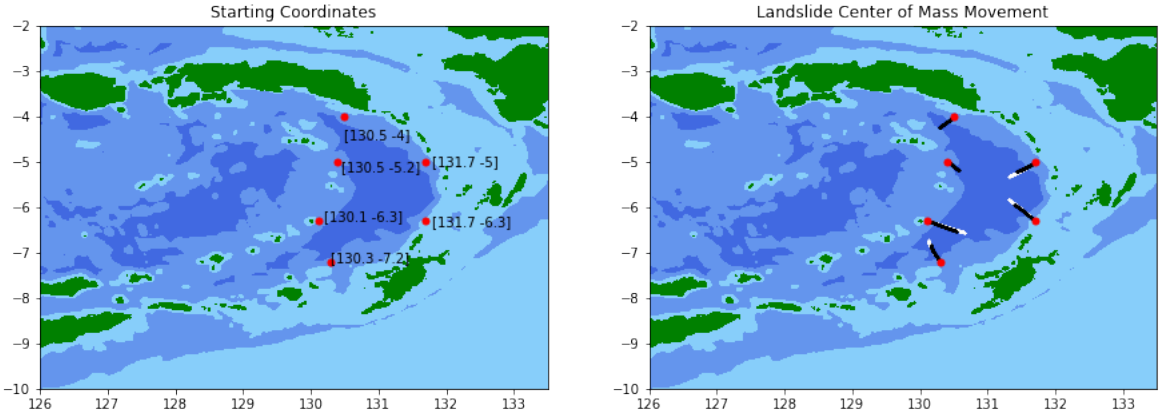

Figure 7.1: (Left): Starting points for chains. Chains starting at [130.5,-4] and [130.5,-5.2] start with reduced volume due to proximity to Banda Neira. (Right): Center of mass landslide movement at initial parameters. Black points represent slides with initial velocities of 25 and white points represent slides with initial velocity of 75.

We choose friction coefficients based on what is physically reasonable. Here, $f = .005$ and C_D is of the order of .002 [23]. We use rough bathymetry data to estimate the angle of descent of the slide. This may make the slide move artificially fast and so we choose $C_D = .009$.

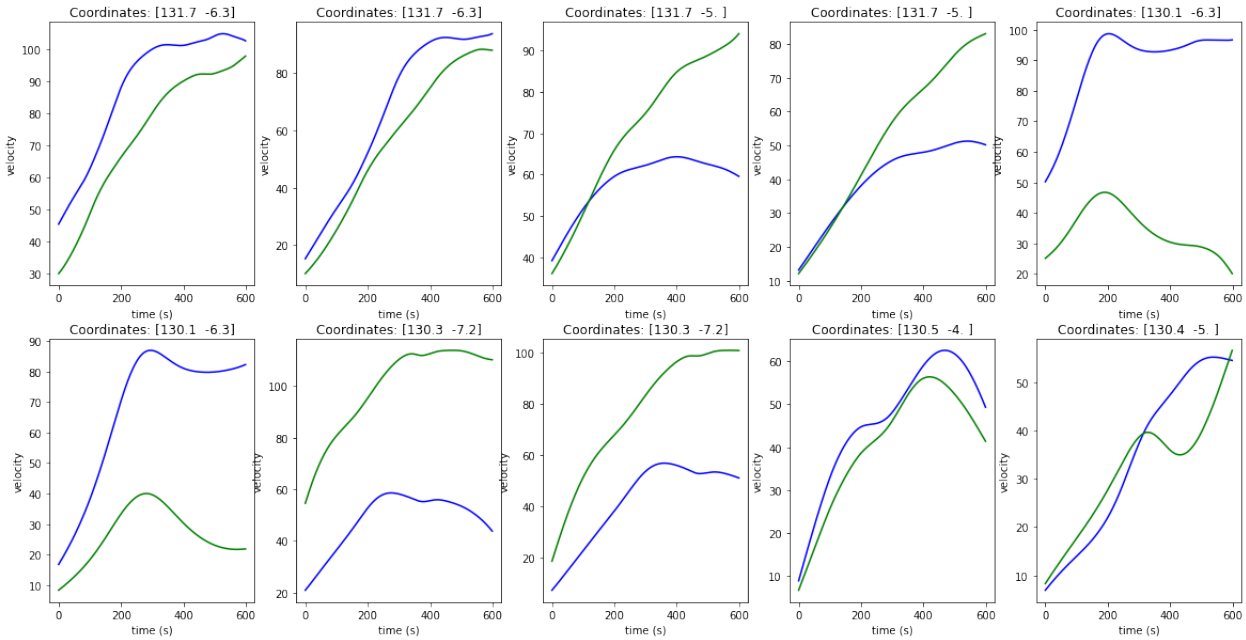

Figure 7.2: Velocity of landslides from initial parameters. We see that the slides velocity increases as the mass of the landslide moves downhill and then slows as the slide reaches the floor of the basin. Landslide velocities are highly dependent on friction coefficients.

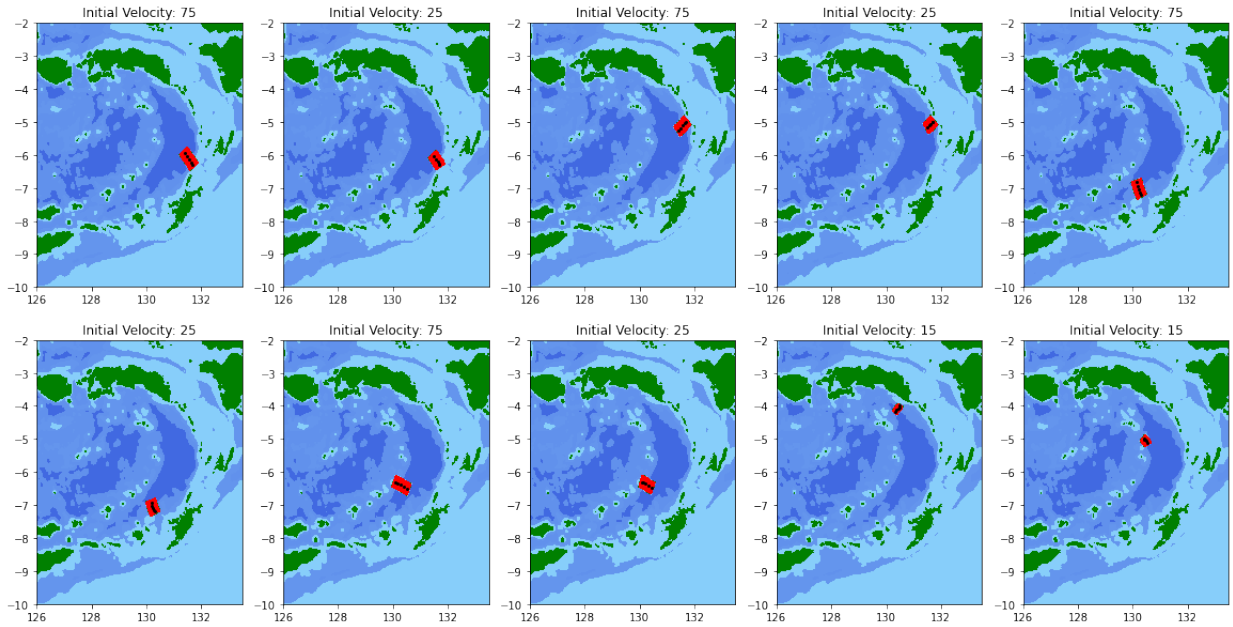

Figure 7.3: Initial landslide mass movement. A 'box' of landslide mass is moved across 5 discrete points from the slide center of mass movement.

7.1 Choosing a Proposal Kernel

To sample from our chains using the Metropolis-Hasting algorithm we must choose a proposal kernel $q(.|\theta_t)$. This proposes a new potential sample θ_{t+1} which will then be accepted or rejected. We use the random walk proposal kernel, i.e. the kernel is given by a Gaussian distributed random variable with covariance matrix Σ, i.e. $N(0, \Sigma)$. Choosing the proposal kernel as well as the parameter Σ is an active area of research. It is generally accepted that proposal kernels which give acceptance rates of approximately .234 are preferred for random walk MCMC [39]. We collected 800 samples per chain with three different proposal kernels to try and determine the 'optimal' values of Σ.

7.1.1 Kernel 1. Parameters for this proposal distribution are found in Table 7.2.

	Lat.	Lon.	Initial Velocity	Volume	Thickness	Aspect Ratio
Standard Dev.	. 075	.075	.5	10000000	0.3	0.01

Table 7.2: Standard deviation for kernel 1.

Figure 7.4 shows that acceptance rates are between 0.1 and 0.3 for this kernel except for chain 5 and chain 8 which have acceptance rates close to zero. This implies that these chains are not able to find anything that matches the data. We also see, looking at the parameter values for volume and initial velocity, that our chains are not mixing well. In particular, not only do the longitude-latitude locations not mix, but the volume of each chain appears to be stuck and unable to transition to different values. Hence we increase the standard deviation of the proposal distribution to try and get the chains to mix a bit more.

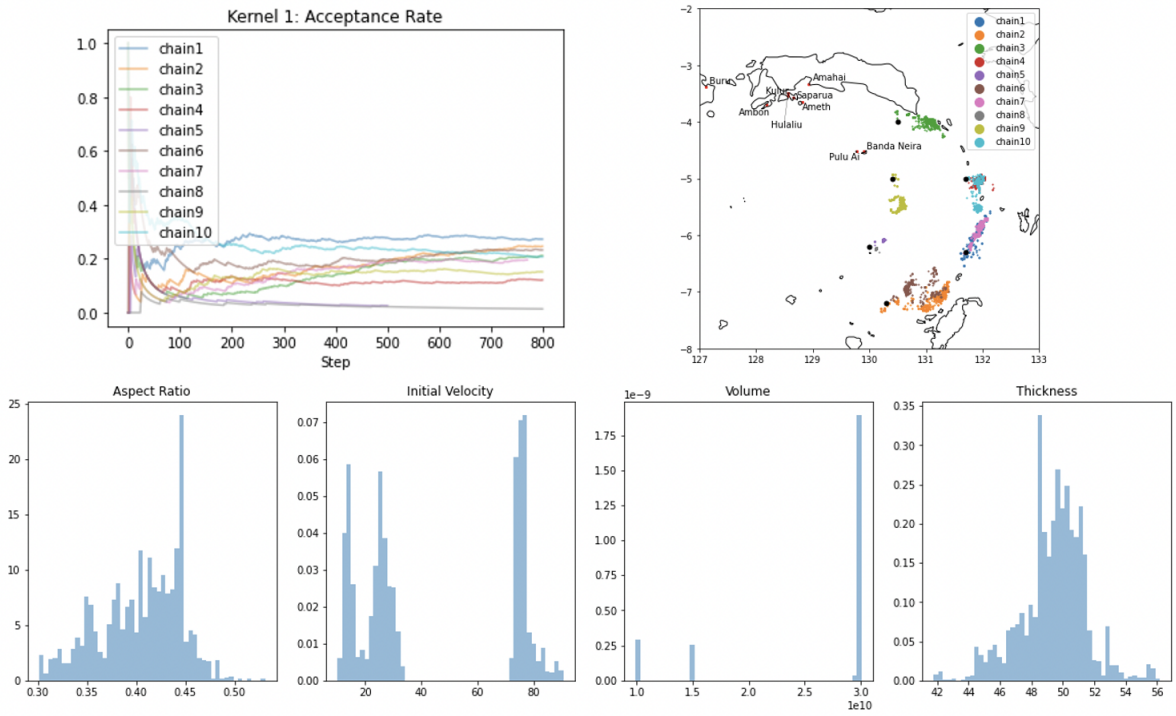

Figure 7.4: 800 samples in each chain are illustrated for proposal kernel 1. (Upper Left): Acceptance rates over time for all 10 chains. (Upper Right): Latitude/longitude movement for all 10 chains. Note that at least up to the 800 samples taken here, none of these chains are mixing with each other at least in longitude and latitude. (Bottom): Histogram for different parameter values of samples from all 10 chains.

7.1.2 Kernel 2. This proposal kernel increases the step size for the initial velocity, volume, and the thickness. This leads to greater mixing for the volume and initial velocity, and now there is only one chain with an acceptance rate close to zero. More importantly the volume parameter is moving and searching over viable choices of parameters and no longer fixated on its initial setting.

	Lat.	Lon.	Initial Velocity	Volume	Thickness	Aspect Ratio
Standard Dev.	.075	.075	.75	225000000	.375	0.01

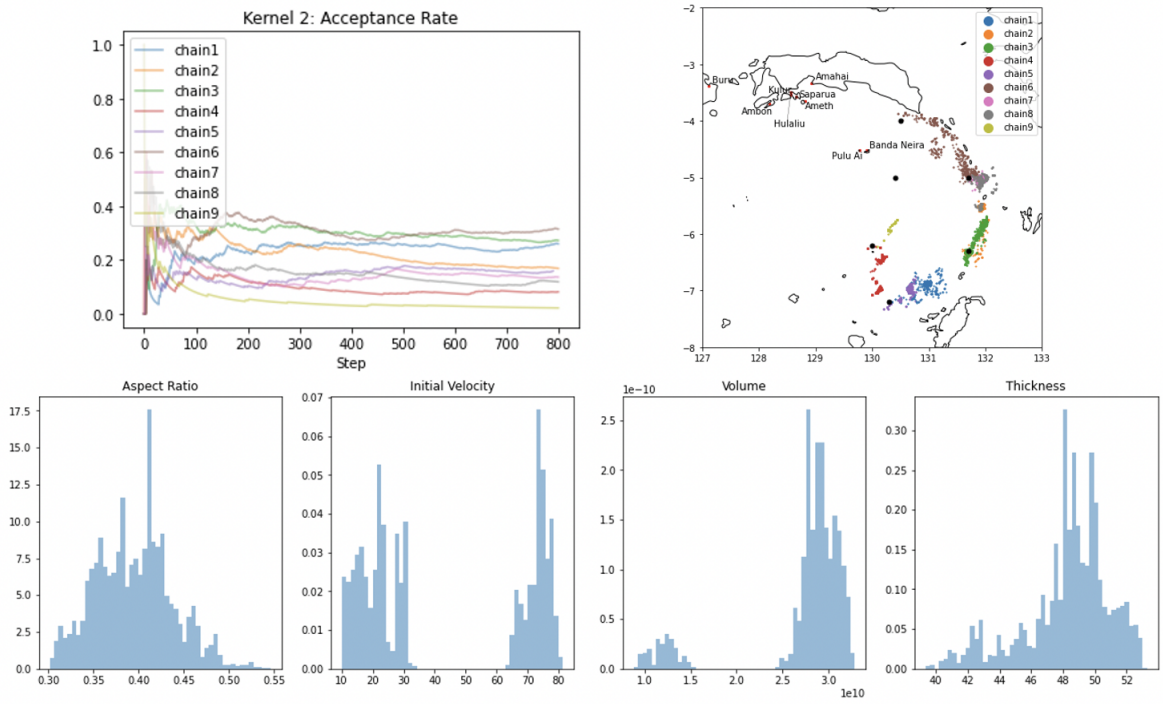

Figure 7.5: (Upper Left): Acceptance rates over time for all 10 chains. (Upper Right): Latitude/longitude movement for all 10 chains. (Bottom): Histogram for different parameter values of samples from all 10 chains.

7.1.3 Kernel 3. For the final proposal kernel we increased the step size for the volume, initial velocity, and thickness parameters one more time. Here we see improved mixing as well as higher acceptance rates, between 0.2 and 0.3. This is the kernel used for the remainder of the results presented. Most relevant, all of the landslide parameters are now truly searching over the entire allowable region.

	Lat.	Lon.	Initial Velocity	Volume	Thickness	Aspect Ratio
Standard Dev.	.075	.075	.95	600000000	.5	0.001

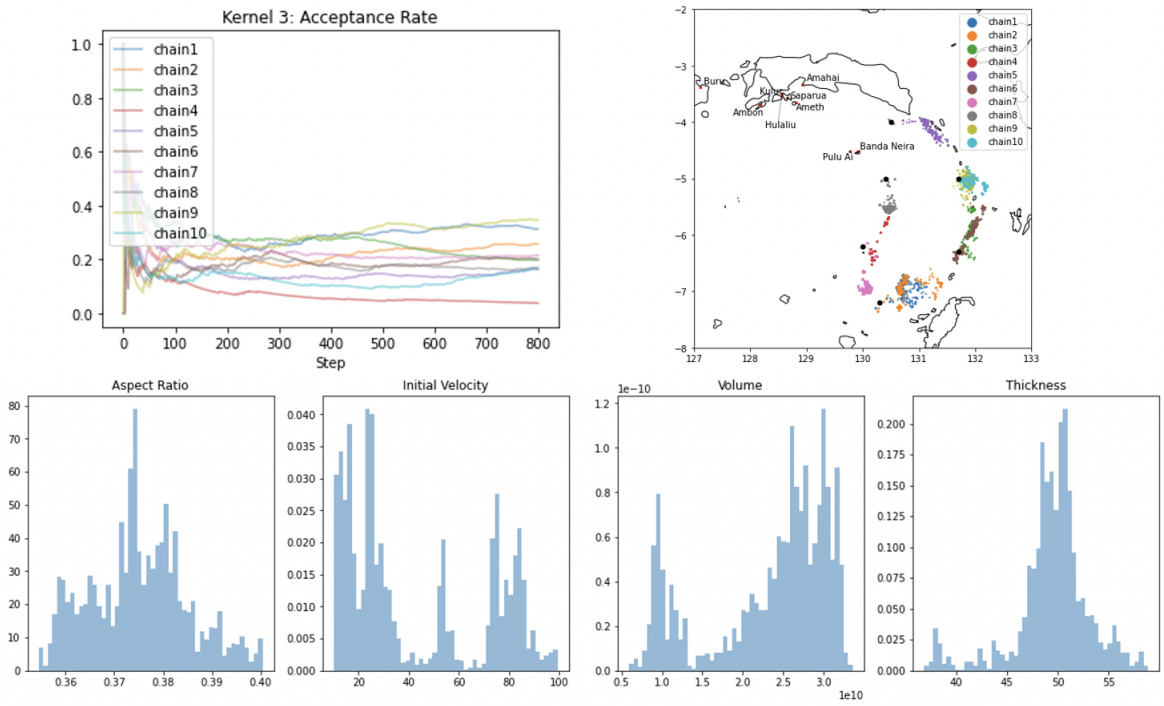

Figure 7.6: (Upper Left): Acceptance rates over time for all 10 chains. (Upper Right): Latitude/longitude movement for all 10 chains. (Bottom): Histogram for different parameter values of samples from all 10 chains.

7.2 Results

After settling on proposal kernel 3 we collected approximately 30,000 samples over ten different chains initialized as mentioned above. Depending on computational resources each sample took between 5.5 and 9 minutes to run. The posterior logpdf over latitude/longitude as well as individual chain movement is shown in Figure 7.7. The posterior shows two areas of high probability. One on the western side of the Weber Deep between starting coordinates $[130.1, -6.3]$ and $[130.5, -5.2]$ and the other on the eastern side of the Weber Deep between starting coordinates $[131.7, -5]$ and $[131.7, -6.3]$. The two chains starting on the south west side of the Weber Deep near $[130.1, -6.3]$ had the most difficult time matching the data. Both of these chains were started at a volume of 30 km^3 and produced waves too large to

match the data. One of these chains, shown in Figure 7.7 in red, had a very low acceptance rate and never provided a good match to the data. It is uncertain if with more samples the volume would decrease to a similar level as the chain starting at $[130.5, -5.2]$ which ends in a similar place, and does provide a decent fit to the data. The other chain starting at $[130.1, -6.3]$, shown in figure 7.7 in pink crossed over an area of low prior probability to the eastern side of the Weber Deep where the simulated tsunami matches the observations far better.

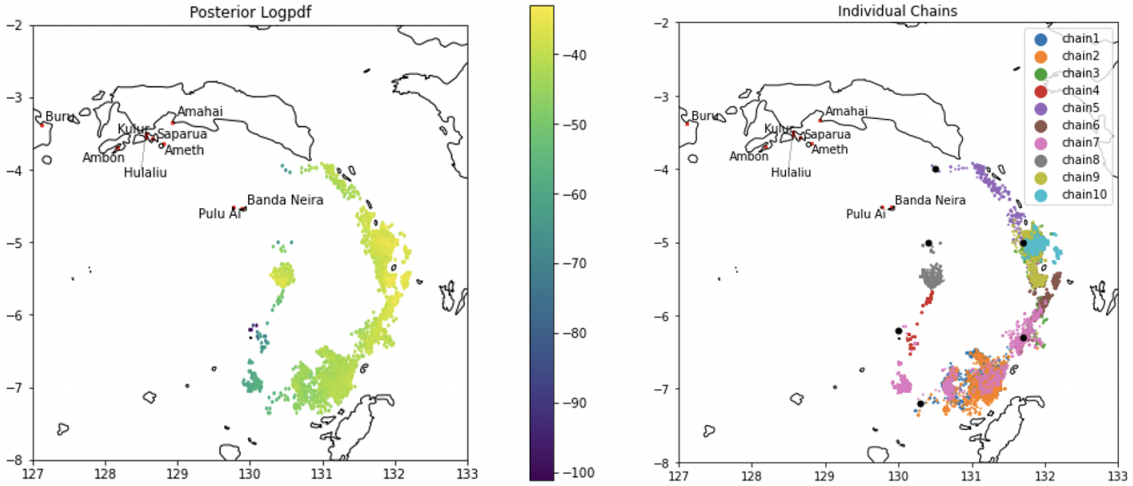

Figure 7.7: (Left): Posterior distribution on latitiude-longitude constructed using MCMC samples. Note the two areas of high probability on the western and eastern side of the Weber Deep. (Right): MCMC samples by chain. Note chain7, shown in pink, makes it's way from the western side all the way over to the area of high probability on the eastern side.

These initial results appear to produce wave heights that are reasonable when compared to the data as depicted in the histograms in Figures 7.8 and 7.9. We note that wave heights produced during MCMC simulations recorded at the island of Kulur do not quite match the observational distributions. This does not raise a significant amount of concern for two reasons. First, observational distributions are constructed based on anecdotal historical accounts and are subject to error. We see the entire histogram for wave heights at Kulur is in an area of low but not zero probability. Histograms in an area of zero probability

are more likely to signify a mismatch with the data. One such example are the histograms corresponding to the Fores arrival times and Walanae/Flores wave heights at the island of Bulakumba shown in Figure 3.2a. Second, we do not want the samples to match observational distributions precisely. In addition to our likelihood, which is dependent on our observational distributions, our posterior samples should be affected by the prior which dictates what is physically feasible. Additionally, an exact fit could signify that we may be 'overfitting' in the sense that there are enough free parameters in the model that any tsunami can be simulated.

We also note many of the observable histograms shown in Figures 7.8 and 7.9 indicate two distinct peaks. This is most apparent for samples describing wave heights, arrival times and inundation levels at Band Neira as well as arrival times and inundation levels for Saparua.

These dual peaks correspond to samples produced by the two areas of high likelihood on the eastern as well as the western side of the Weber Deep.

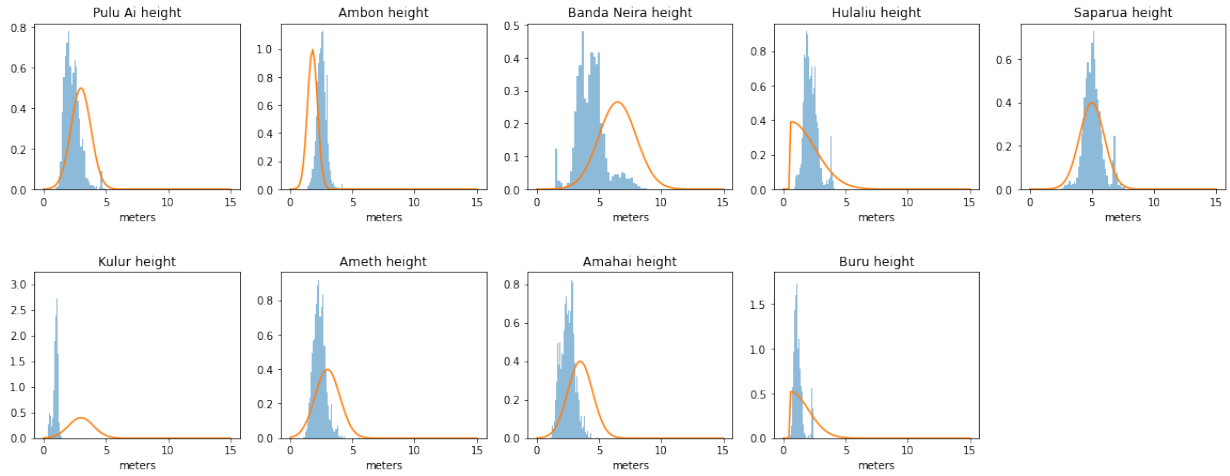

Figure 7.8: Wave heights generated from tsunami simulation during the MCMC process, in blue, compared to observational distributions shown in orange.

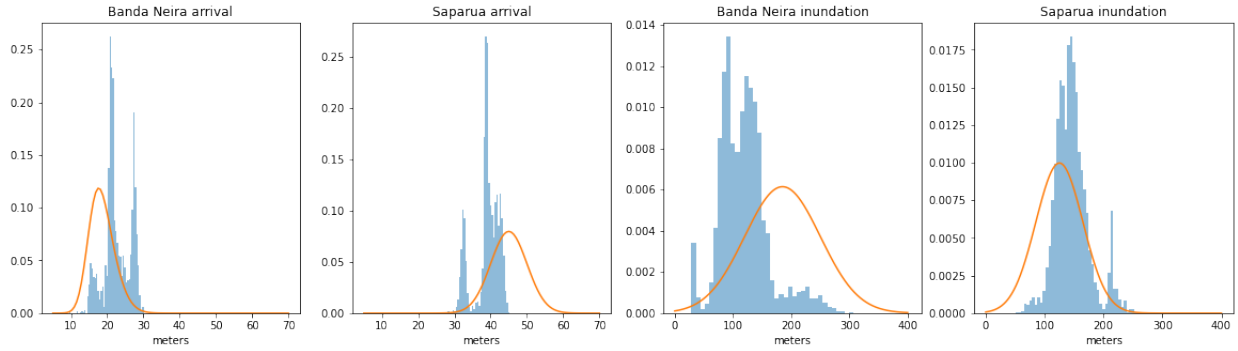

Figure 7.9: Arrival times and inundation levels generated from tsunami simulation during the MCMC process, in blue, compared to observational distributions shown in orange.

7.2.1 Resampling. After computing these initial results we resampled the chains with replacement according to their final posterior probabilities and restarted the sampling procedure for each chain. The longitude-latitude locations of the selected chains are shown in Figure 7.10. In total, we initiated 10 different MCMC chains. Again, these ran simultaneously on BYU's supercomputer in the Office of Research Computing on 24 cores. We have, and show results for, 30,000 samples collected from our resampled chains, 3,000 samples per chain. We are still currently collecting samples and our research group will continue to collect samples over the next few months to ensure convergence of the posterior. Ultimately, the posterior will be comprised of hundreds of thousands of samples.

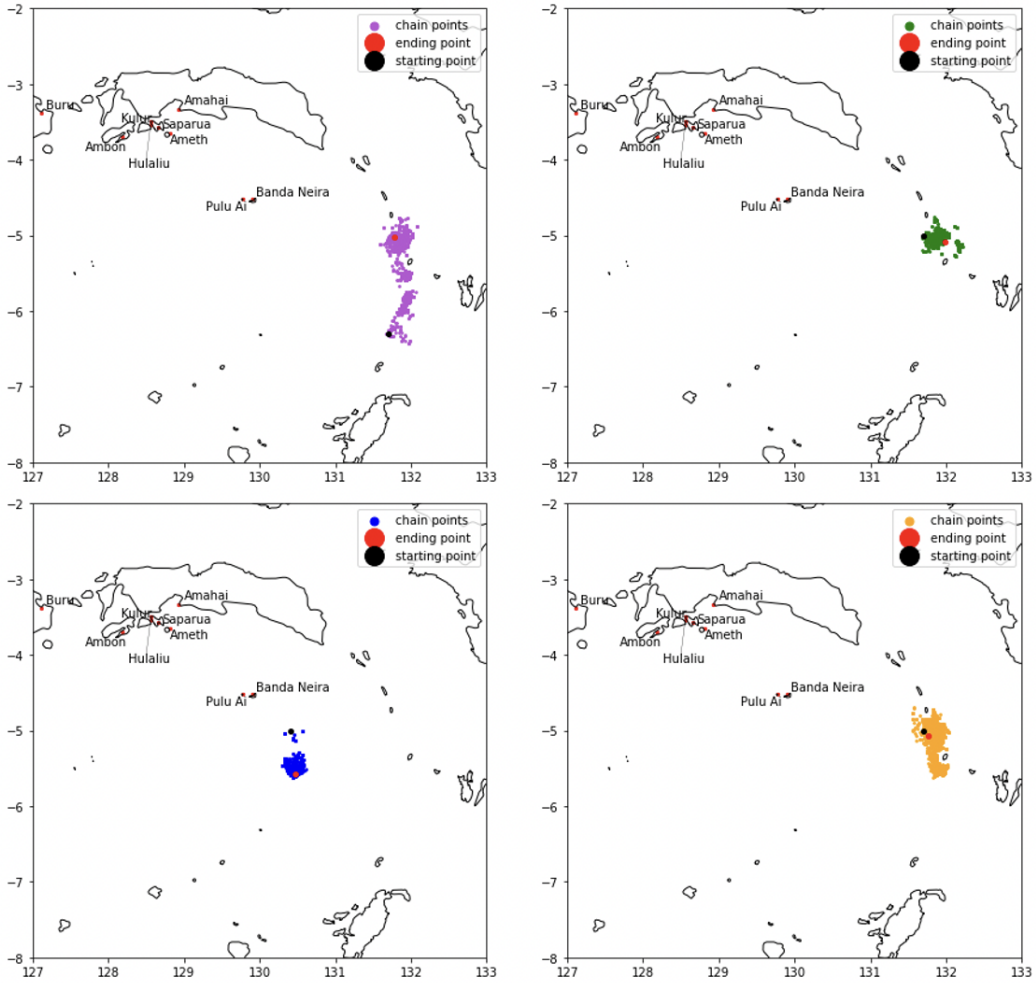

Figure 7.10: Chains chosen for resampling. The starting point is shown in black and the last sample in each chain is shown in red. The chain shown in blue was resampled from once, orange twice, green twice, and purple five times.

We see our posterior distribution for longitude and latitude, shown in Figure 7.11 is concentrated around the two locations of high likelihood as seen in Figure 7.7. It is more apparent in the resampled posterior that landslides starting on the eastern side of the Weber Deep provide a better fit to the data.

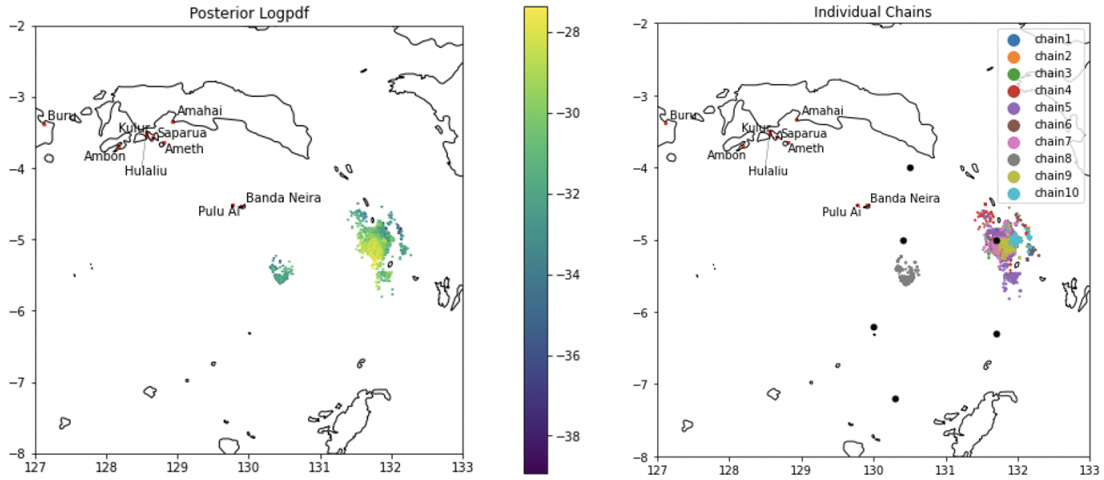

Figure 7.11: (Left): Posterior distribution on latitiude-longitude constructed using MCMC samples. Note the two areas of high probability on the western and eastern side of the Webber deep. (Right): MCMC samples by chain.

Our posterior for landslide parameters is shown in Figure 7.12. The samples for volume and aspect ratio seem to collect around 20 km^3 and .385 respectively potentially indicating convergence of those distributions. More interestingly, samples for initial velocity and thickness do not gravitate towards a single value. Both of these distributions have two peaks. This is partially explained by the chains on the eastern and western side of the Weber Deep. However, there are more samples in each peak than can be explained by the single chain in the west. One explanation is that wave heights, arrival times and inundation levels are not affected greatly by either the initial velocity of the landslide or the thickness, total volume holds more import. This is also supported by the fact that the resampling procedure chose chains with varying initial velocities and thicknesses. However, it is hard to draw a firm conclusion until more samples are collected.

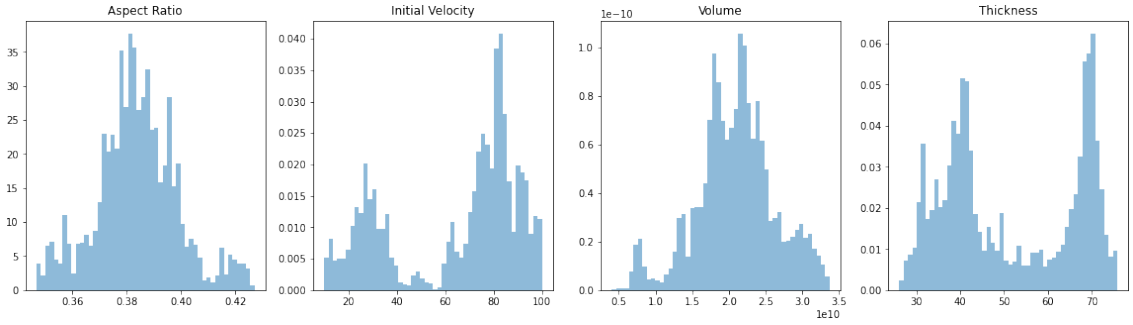

Figure 7.12: Posterior distribution on landslide parameters constructed using MCMC samples.

Results for wave heights, arrival times and inundation levels are similar to the results shown before resampling in Figures 7.8 and 7.9. Again, we see distributions with two peaks. These include wave heights arrival times and inundation levels at Banda Neira as well as Saparua arrival times. Here, these peaks are solely due to the two areas of high likelihood in the locational posterior. The majority of samples come from east of the Weber Deep while the smaller peaks correspond to samples west of the Weber Deep. We see the smaller peak, corresponding to the west have earlier arrival times at Banda Neira and Saparua as well as higher innundation levels at Banda Neira. This is due to the close proximity of samples on the west of the Weber Deep to the islands of Banda Neira and Saparua.

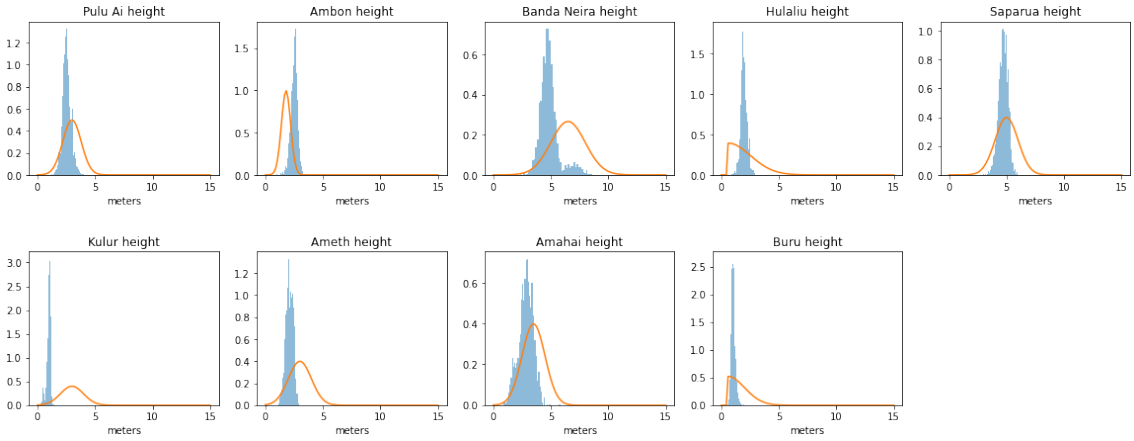

Figure 7.13: Wave heights generated from tsunami simulation during the MCMC process, in blue, compared to observational distributions, in orange.

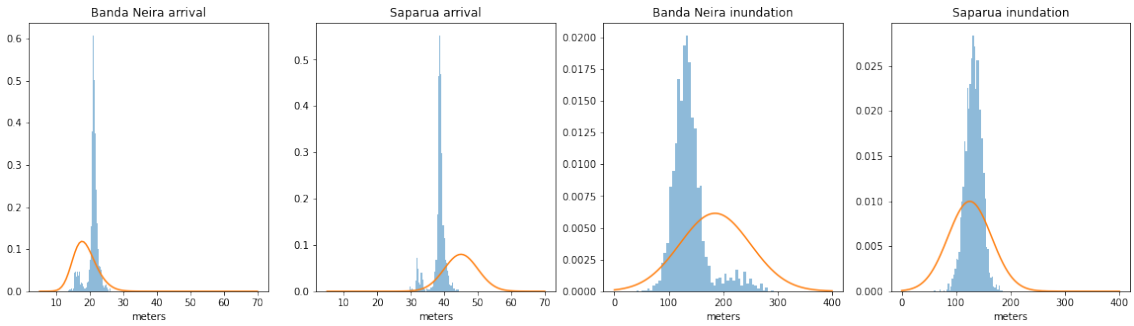

Figure 7.14: Arrival times and inundation levels generated from tsunami simulation during the MCMC process, in blue, compared to observational distributions, in orange.

Chapter 8. Conclusion

Over all, the landslide hypothesis appears to provide a reasonable fit to the accounts of the 1852 tsunami. We see that MCMC samples are not far off from observational histograms after taking into account information from the prior. The one caveat being, due to limited knowledge of submarine landslides it is difficult to say if the landslides that best match the data are physically feasible. The most likely landslides accelerate up to a velocity of around

100 m/s within a 10 minute period. Friction coefficients and model parameters can be tuned to decrease certain model behaviors. For example, friction coefficients can be tuned ouside of realistic values to compensate for rough bathymetry data which is also somewhat unrealistic. This would decrease acceleration. For this work, while some slides may be on the edge of what is reasonable, we tune parameters, such as friction coefficients, within values believed to be physically accurate.

Chapter 9. Future Work

This project lends itself to two main areas of future work. The first of these is to create a combined earthquake/landslide model. Combined models such as this have been successfully used to match observational data when a single source landslide model cannot. One such tsunami occurred northwest of the Indian Ocean. Single source models were not able to reproduce the observed near-field runup of 10–12 m. However, a coupled earthquake-landslide model was able to math observational data [40]. Additionally, an earthquake of MW 7.5 was recorded in northwestern Indonesia, in 2018, along with a tsunami which caused significant destruction in Palu City. Observations suggest that the earthquake alone did not generate the tsunami. Multiple submarine landslides are hypothesized to have occurred in Palu Bay which contributed to the destructive power of the tsunami [41].

This is especially relevant when discussing the 1820 event as described in [18] and summarized in Section 3.1. The data generated from the earthquake based tsunami model did not match the observational distributions as closely as desired. This was most apparent when looking at the wave heights and arrival times at the gauge location by the island of Bulukumba. One way to account for these discrepancies would be to have a local slide by Bulukumba increasing wave heights locally, but not throughout the entire Flores Sea.

The second, and perhaps most natural area of future work is to decrease the computational effort required to create a posterior. Our research group is currently looking at Hamiltonian Monte Carlo methods [42]. This is an MCMC scheme that accepts samples

at a higher rate than the default 23.4%. Hamiltonian Monte Carlo is based on ideas from Hamiltonian dynamics. Hamiltonian dynamics describe the motion of a particle over a frictionless surface. Hamiltonian Monte Carlo requires the gradient of the model. This motion replaces the proposal kernel in random walk Monte Carlo. We are not able to compute exact gradients of GeoClaw and so rely on surrogate gradients. A neural network was trained on the samples generated by GeoClaw and analyzed by [12]. After training, the root mean squared error of the test data was ≈ 0.331. Details on the construction and training of this network can be found in [43]. Gradients of this network are currently being used as a surrogate in preliminary tests for a Hamiltonian Monte Carlo scheme [44].

Bibliography

[1] Kevin McCue et al. Seismic hazard mapping in Australia, the Southwest Pacific and Southeast Asia. 1999.

[2] Ron Harris and Jonathan Major. Waves of destruction in the East Indies: the Wichmann catalogue of earthquakes and tsunami in the Indonesian region from 1538 to 1877. *Geological Society, London, Special Publications*, 441(1):9–46, 2017.

[3] Latief Hamzah, Nanang T Puspito, and Fumihiko Imamura. Tsunami catalog and zones in Indonesia. *Journal of Natural Disaster Science*, 22(1):25–43, 2000.

[4] Yoshiaka Kawata, Boyd C Benson, José C Borrero, José L Borrero, Hugh L Davies, Willem P de Lange, Fumihiko Imamura, Horst Letz, Jonathan Nott, and Costas E Synolakis. Tsunami in Papua New Guinea was as intense as first thought. *Eos, Transactions American Geophysical Union*, 80(9):101–105, 1999.

[5] Bruce Charles Heezen and William Maurice Ewing. Turbidity currents and submarine slumps, and the 1929 Grand Banks [Newfoundland] earthquake. *American journal of Science*, 250(12):849–873, 1952.

[6] S Assier-Rzadkieaicz, Ph Heinrich, PC Sabatier, B Savoye, and JF Bourillet. Numerical modelling of a landslide-generated tsunami: the 1979 Nice event. *Pure and Applied Geophysics*, 157:1707–1727, 2000.

[7] Tom Bugge, RH Belderson, and NH Kenyon. The Storegga slide. *Philosophical Transactions of the Royal Society of London. Series A, Mathematical and Physical Sciences*, 325(1586):357–388, 1988.

[8] Carl B Harbitz, Finn Løvholt, and Hilmar Bungum. Submarine landslide tsunamis: how extreme and how likely? *Natural Hazards*, 72:1341–1374, 2014.

[9] Finn Løvholt, G Pedersen, Carl Bonnevie Harbitz, Sylfest Glimsdal, and Jihwan Kim. On the characteristics of landslide tsunamis. *Philosophical Transactions of the Royal Society A: Mathematical, Physical and Engineering Sciences*, 373(2053):20140376, 2015.

[10] Steven N Ward and Simon Day. Suboceanic landslides. *2002 yearbook of science and technology*, pages 349–352, 2002.

[11] Phil R Cummins, Ignatius R Pranantyo, Jonathan M Pownall, Jonathan D Griffin, Irwan Meilano, and Siyuan Zhao. Earthquakes and tsunamis caused by low-angle normal faulting in the Banda Sea, Indonesia. *Nature Geoscience*, 13(4):312–318, 2020.

[12] Hayden Ringer, Jared Whitehead, Justin Krometis, Harris Ronald A, Nathan Glatt-Holtz, Spencer Giddens, Claire Ashcraft, Garret Carver, Adam Robertson, McKay Harward, Joshua Fullwood, Kameron Lightheart, Ryan Hilton, Ashley Avery, Cody Kesler, Martha Morrise, and Michael Hunter Klein. Methodological reconstruction of historical seismic events from anecdotal accounts of destructive tsunamis: a case study for the great 1852 banda arc mega-thrust earthquake and tsunami. 2021.

[13] Jari Kaipio and Erkki Somersalo. *Statistical and computational inverse problems*, volume 160. Springer Science & Business Media, 2006.

[14] David M Blei, Alp Kucukelbir, and Jon D McAuliffe. Variational inference: A review for statisticians. *Journal of the American statistical Association*, 112(518):859–877, 2017.

[15] W Keith Hastings. Monte Carlo sampling methods using Markov chains and their applications. 1970.

[16] Nicholas Metropolis, Arianna W Rosenbluth, Marshall N Rosenbluth, Augusta H Teller, and Edward Teller. Equation of state calculations by fast computing machines. *The journal of chemical physics*, 21(6):1087–1092, 1953.

[17] Nizar Bouguila and Wentao Fan. *Mixture models and applications*. Springer, 2020.

[18] R.A. Harris C. Ashcraft J. A. Krometis I. Sorensen T. Paskett, J. P. Whitehead and R. Wonnacott. tale of two faults: Statistical reconstruction of the 1820 Flores Sea earthquake using tsunami observations alone. *submitted*.

[19] Randall J LeVeque and David L George. High-resolution finite volume methods for the shallow water equations with bathymetry and dry states. In *Advanced numerical models for simulating tsunami waves and runup*, pages 43–73. World Scientific, 2008.

[20] Randall J LeVeque, David L George, and Marsha J Berger. Tsunami modelling with adaptively refined finite volume methods. *Acta Numerica*, 20:211–289, 2011.

[21] Frank I González, Randall J LeVeque, Paul Chamberlain, Bryant Hirai, Jonathan Varkovitzky, and David L George. Validation of the geoclaw model. In *NTHMP MMS Tsunami Inundation Model Validation Workshop. GeoClaw Tsunami Modeling Group*, 2011.

[22] Marsha J Berger, David L George, Randall J LeVeque, and Kyle T Mandli. The GeoClaw software for depth-averaged flows with adaptive refinement. *Advances in Water Resources*, 34(9):1195–1206, 2011.

[23] E Pelinovsky and A Poplavsky. Simplified model of tsunami generation by submarine landslides. *Physics and Chemistry of the Earth*, 21(1-2):13–17, 1996.

[24] Jeffrey Humpherys, Tyler J Jarvis, and Emily J Evans. *Foundations of Applied Mathematics, Volume I: Mathematical Analysis*, volume 152. SIAM, 2017.

[25] A Wichmann. The earthquakes of the Indian archipelago to 1857. *Verhandl. Koninkl. Akad. van Wetenschappen, 2nd sec*, 20(4):1–193, 1918.

[26] A Wichmann. The earthquakes of the Indian archipelago from 1858 to 1877. *Verhandl. Koninkl. Akad. van Wetenschappen, 2nd sec*, 22(5):1–209, 1922.

[27] Anders Elverhoi, Hedda Breien, Fabio V De Blasio, Carl B Harbitz, and Matteo Pagliardi. Submarine landslides and the importance of the initial sediment composition for run-out length and final deposit. *Ocean Dynamics*, 60:1027–1046, 2010.

[28] Monty A Hampton, Homa J Lee, and Jacques Locat. Submarine landslides. *Reviews of geophysics*, 34(1):33–59, 1996.

[29] Steven N Ward. Landslide tsunami. *Journal of Geophysical Research: Solid Earth*, 106(B6):11201–11215, 2001.

[30] Roger Urgeles and Angelo Camerlenghi. Submarine landslides of the Mediterranean Sea: Trigger mechanisms, dynamics, and frequency-magnitude distribution. *Journal of Geophysical Research: Earth Surface*, 118(4):2600–2618, 2013.

[31] Jason D Chaytor, Uri S ten Brink, Andrew R Solow, and Brian D Andrews. Size distribution of submarine landslides along the US Atlantic margin. *Marine Geology*, 264(1-2):16–27, 2009.

[32] SM Abadie, JC Harris, ST Grilli, and R Fabre. Numerical modeling of tsunami waves generated by the flank collapse of the Cumbre Vieja Volcano (La Palma, Canary Islands): Tsunami source and near field effects. *Journal of Geophysical Research: Oceans*, 117(C5), 2012.

[33] Isaac V Fine, Alexander B Rabinovich, BD Bornhold, RE Thomson, and Evgueni A Kulikov. The Grand Banks landslide-generated tsunami of November 18, 1929: preliminary analysis and numerical modeling. *Marine Geology*, 215(1-2):45–57, 2005.

[34] CB Harbitz. Model simulations of tsunamis generated by the Storegga slides. *Marine geology*, 105(1-4):1–21, 1992.

[35] Eric L Geist, Patrick J Lynett, and Jason D Chaytor. Hydrodynamic modeling of tsunamis from the Currituck landslide. *Marine Geology*, 264(1-2):41–52, 2009.

[36] F Løvholt, G Pedersen, and G Gisler. Oceanic propagation of a potential tsunami from the La Palma Island. *Journal of Geophysical Research: Oceans*, 113(C9), 2008.

[37] Jessica A Reid and Walter D Mooney. Tsunami Occurrence 1900–2020: A Global Review, with Examples from Indonesia. *Pure and Applied Geophysics*, pages 1–23, 2022.

[38] Davide Gamboa, Rachid Omira, and Pedro Terrinha. A database of submarine landslides offshore West and Southwest Iberia. *Scientific Data*, 8(1):185, 2021.

[39] Andrew Gelman, Walter R Gilks, and Gareth O Roberts. Weak convergence and optimal scaling of random walk Metropolis algorithms. *The annals of applied probability*, 7(1):110–120, 1997.

[40] Mohammad Heidarzadeh and Kenji Satake. A combined earthquake–landslide source model for the Tsunami from the 27 November 1945 M w 8.1 Makran earthquake. *Bulletin of the Seismological Society of America*, 107(2):1033–1040, 2017.

[41] Alexey Androsov, Sven Harig, and Natalja Rakowsky. Simulating Landslide Generated Tsunamis in Palu Bay, Sulawesi, Indonesia. *Geosciences*, 13(3):72, 2023.

[42] Radford M Neal et al. MCMC using Hamiltonian dynamics. *Handbook of markov chain monte carlo*, 2(11):2, 2011.

[43] James Griffin. Tsunami sensitivity quantification using neural networks. Master's thesis, 2022.

[44] Jake Callahan. Hamiltonian Monte Carlo for Reconstructing Historical Earthquake-induced Tsunamis. Master's thesis, 2023.